Realistic modeling of ephaptic fields in the human brain

Giulio Ruffini[1,2,3*], Ricardo Salvador[2], Ehsan Tadayon[4], Roser Sanchez-Todo[2], Alvaro Pascual-Leone[4,5], Emiliano Santarnecchi[4]

[1] Neuroelectrics Corporation, 210 Broadway, 02139 Cambridge, MA, USA

[2] Neuroelectrics Barcelona, Avda. Tibidabo, 47 bis, 08035 Barcelona, Spain

[3] Starlab Barcelona, Avda. Tibidabo, 47 bis, 08035 Barcelona, Spain

[4] Berenson-Allen Center for Noninvasive Brain Stimulation, Beth Israel Deaconess Medical Center and Harvard Medical School, Boston, MA, USA

[5] Institut Guttmann, Universitat Autònoma de Barcelona, Barcelona, Spain

*To whom correspondence should be addressed; E-mail: giulio.ruffini@neuroelectrics.com.

Running title: Modeling Ephaptic Fields

Figures: 5

Tables: 2

Financial disclosures. GR is co-founder of Neuroelectrics; RS and RS-T work at Neuroelectrics, a company that produces EEG and tCS systems. The other authors report no conflict of interest.

Corresponding author:

Giulio Ruffini

Neuroelectrics Corporation

210 Broadway, Suite 201

02139 Cambridge, MA, USA

Mobile: +1 6177 899 6911

giulio.ruffini@neuroelectrics.com

Abstract

Several decades of research suggest that weak electric fields may influence neural processing, including those induced by neuronal activity and recently proposed as substrate for a potential new cellular communication system, i.e., ephaptic transmission. Here we aim to map ephaptic activity in the human brain and explore its trajectory during aging by characterizing the macroscopic electric field generated by cortical dipoles using realistic finite element modeling. We find that modeled endogenous field magnitudes are comparable to those in measurements of weak but functionally relevant endogenous fields and to those generated by noninvasive transcranial brain stimulation, therefore possibly able to modulate neuronal activity. Then, to evaluate the role of self-generated ephaptic fields in the human cortex, we adapt an interaction approximation that considers the relative orientation of neuron and field to derive the membrane potential perturbation in pyramidal cells. Building on this, we define a simplified metric (EMOD1) that weights dipole coupling as a function of distance and relative orientation between emitter and receiver and evaluate it in a sample of 401 realistic human brain models from subjects aged 16-83. Results reveal that ephaptic modulation follows gyrification patterns in the human brain, and significantly decreases with age, with higher involvement of sensorimotor regions and medial brain structures. By providing the means for fast and direct interaction between neurons, ephaptic modulation likely contributes to the complexity of human function for cognition and behavior, and its modification across the lifespan and in response to pathology.

1 INTRODUCTION

Jefferys (*1*) defined population electric field effects as those "in which the synchronous activity of populations of neurons causes large electric fields that can affect the excitability of suitably oriented, but not closely neighboring, neurons". The literature refers to these, loosely, as "ephaptic interactions". Traveling at the speed of electromagnetic radiation, self-generated ephaptic fields provide the means for fast and direct interaction between neurons, enabling new mechanisms for communication and computation that remain incompletely understood. Although much faster than chemical synaptic transmission and with a longer range than electrical synaptic communication in gap junctions, electromagnetic waves travel slower in biological media than in vacuum. Table S1 in Supplementary Materials summarizes the relevant electromagnetic properties of tissues in the brain, including propagation velocity.

Work in the last decades has shown that neuronal circuits are surprisingly sensitive to weak endogenous or exogenous low frequency (0–100 Hz) electric fields (> 0.1 V/m). For example, Frohlich et al (2) showed that exogenous direct current (DC) and low frequency alternating current (AC) electric fields modulate neocortical network activity in slices with a threshold of 0.5 V/m. They also found effects from the application of exogenous fields mimicking endogenous fields recorded from the slices. More recent research has further established the role of ephaptic interactions and the sensitivity of neuronal populations to weak fields both in-vitro and in-silico. In particular, it demonstrates that ephaptic fields are capable of mediating the propagation of self-regenerating slow (~0.1 m/s) neural waves (*3, 4*) and that externally applied extracellular electric fields with amplitudes in the range of endogenous fields are sufficient to modulate or block the propagation of this activity both in vitro and in silico models *(5)*. Field amplitudes in the range of 0.1–5 V/m have also been shown to produce physiological effects in primates using transcranial electrical current stimulation (see, e.g., (6) for recent results in nonhuman primates). Table S2 in Supplementary Materials provides an overview spanning six decades of in-vivo and in-vitro research on the physiological impact of weak, low frequency (< 100 Hz) electric fields—both exogenous and endogenous.

Here we focus on endogenous fields that may contribute to short-range communication at or above millimeter scales, that is, not ultra-local ephaptic effects coupling adjacent neurons. The

generation of fields capable of effectively bridging such distances necessitates the synchronized activity of neuronal populations (*7*, *8*) radiating from cortical patches, which occurs at frequencies below about 100 Hz (the "EEG regime") and with spatial correlation scales in the order of a centimeter. We will call these slow, macroscopic ephaptic fields SEFs for short. As SEFs appear to be of physiological relevance (v. Table S2) and not simply an epiphenomenon, understanding how and where they play a functional role may be necessary for the development of realistic models of neural dynamics and function. Additional motivation for this study derives from seeking a theory for the effects of the weak exogenous electric fields—such as the ones generated by transcranial electrical current stimulation (tCS or tES, as it is sometimes known). At the frequencies of interest here (<100 Hz), both endogenous and exogenous tCS fields are characterized by relatively large spatial correlation scales (of the order of centimeter or more) and low magnitudes (> 0.1 V/m). Gaining a better understanding of ephaptic effects may shed some light on how tCS modulates neural dynamics and, eventually, how to optimize it.

First, we use modern biophysical modeling tools to characterize macroscopic ephaptic fields (i.e., spatially averaged at linear scales >0.1 mm, *v.* (*9*), section 4.3) using realistic head modeling. In the Methods section, we describe how we model the electric fields from EEG generating cortical populations at experimentally observed densities and patch sizes and compare them with those described in available experimental work. We analyze this first in an idealized analytical model, then in a simple 3D model, and, finally, in a realistic brain model derived from an individual MRI.

Based on this, we propose an **ephaptic modulation index** that can be computed on individual from realistic brain models (EMOD) to characterize ephaptic coupling in an individual's brain and a derive a first simplified version for computational convenience (EMOD1). Although existing metrics such as gyrification, cortical thickness or surface area capture some geometric aspects relevant to ephaptic coupling, we take a more physics-grounded approach. We build on existing models for the interaction of weak electric fields and neurons as used in the field of transcranial current electrical stimulation (the "lambda-E" model (*10*)). Considering the cytoarchitecture of the cortex placing pyramidal cells oriented perpendicular to the cortical surface, the lambda-E model indicates that the quantity of relevance to study electric field effects is the normal or orthogonal component of the field to the cortex (E_n).

Finally, we analyze how EMOD1 changes across the lifespan by characterizing it from individual structural MRIs of a large sample of 401 heathy individuals aged 16–83. EMOD1 and structural morphologies such as cortical thickness, surface area and gyrification, were correlated with age, providing a map of brain regions whose potential for ephaptic transmission is significantly affected by aging. Such findings suggest that ephaptic modulation might have relevance for cognitive processing and for the manifestation of pathological conditions involving brain morphometric changes as well alterations of oscillatory patterns (e.g., schizophrenia (*11*), depression (*12*), Alzheimer's Disease (*13*) or Parkinson's (*14*)).

2 RESULTS

2.1 Ephaptic map from cortical patch sources in simplified 3D model

Median sulcal width in human brains across the age span can vary between 0.5 and 5 mm (*15*). Using this as a reference, we first studied the characteristics of endogenous fields in a 3D toy model of a sulcus in the cortex. The electric field distribution in the simplified 3D models for a sulcus width of 1 mm is shown in Figure 2 for the multiple dipole model (middle row, figures c-d) and the single dipole model (bottom row, figures e-f). Dipole strength in the multiple dipole model was set to 0.39 and 0.78 nAm, which results in a dipole strength density per unit area of 0.5 and 1.0 nAm/mm^2 in the modeled 60 mm^2 cortical patch. The dipole strength in the single source model was set to the same value, which results in a physiologically realistic (*16*, *17*) local density of 0.5 and 1.0 nAm/mm^2 in the equivalent area associated to this dipole (60 and 77 mm^2). As can be seen in the figure, in the models with the higher dipole density (1.0 nAm/mm^2), an electric field >0.1 V/m can be observed in the wall opposite to the one where the sources are located. This is observed in both the multiple and single source models, although, as expected, the area in which the electric field is greater than 0.1 V/m is higher in the former than in the latter (the electric field from multiple-source patches decays much slower than the single dipole source case (*7*), p. 37). This effect was only observed in the model with sulcus width of 1 mm. Increasing the sulcus width led to lower electric field values on the opposite sulcal wall. Figure 1 in Supplementary Materials displays the decay of the normal component of the electric field and the electrostatic potential with distance. The decays of V and E_n are well fit by a power function with exponents of −0.66, −0.88 and −2.11, −3.02, respectively, for the multiple source and single source models.

2.2 Ephaptic map from cortical patch sources in realistic head model

Next, we analyzed the electric fields in a realistic head model. For each one of 112 single dipole models, we calculated the decay of E_n with Euclidean distance to the source. For all models, the decay was well fit by a power function, with an exponential of −3.2±0.8 (R^2 of fit was 0.76±0.12). Comparing the decay of the normal component of the electric field with distance in the cortical surface, we see that it is approximately monotonic for the Euclidean distance, as expected, but not for the geodesic distance (see Figure S1 in Supplementary Materials, bottom). This behavior

is expected and a result of surface folding.

For the multiple dipole source patch model, different configurations were tested using 133 dipole node sources, with individual dipole strengths adjusted so that the dipole strength area density was of 0.5 nAm/mm^2 or 1.0 nAm/mm^2. This resulted in individual dipole strengths at each node between 1.9 and 4.0 nAm. We also calculated single node dipole versions of these models, with strengths of 2.1 and 4.2 nAm, which correspond to the same density values in the equivalent (mesh triangle) patch size covered by that dipole. For these source strengths, it is possible to achieve an electric field magnitude of at least 0.1 V/m on the opposite sulcus wall (see Figure 3). This effect is local and dependent on the distance between source and sulcus wall. Using single source models positioned in the narrow part of the sulcus (Figure 3 bottom. b/e) and in the wide part of the sulcus (Figure 3 bottom, c/f) we found that only the former induced a 0.1 V/m electric field on the opposite sulcus wall. These results mimic closely those observed in the simplified volume conductor model discussed previously, since for the chosen study area sulcus separation in the realistic model was 1.4–5.5 mm in the dipole patch region (see Figure S2 in Supplementary Materials). For reference, sulcus width in the human cortex can be less than 1 mm (*15*). Table 1 summarizes the maxima of the electrostatic potential (at scalp level) and the electric field in the GM for all the realistic head the models presented here. See also Figure S10 for the scalp potential map associated to the chosen dipole patch.

Finally, as a check of the realistic model, we investigated the voltage distribution at the scalp induced by a single source dipole on the chosen cortical area with a strength of 100 nAm, which is what reciprocity considerations predict would be required to achieve ~10 μV at scalp level (see Methods). The dipole was aligned to the electric field induced in that node by a montage with CP2 as the anode (1 mA) and T10 as the cathode (−1 mA). The potential difference between electrodes CP2 and T10 was of 13 μV (within the expected bounds of the approximation).

2.3 Ephaptic modulation in the human brain

In order to provide a template map for the distribution of ephaptic modulation in the human brain, as well as for its aging-related trajectory, 401 structural MRIs of healthy participants aged 16-83 yrs. were processed using Freesurfer software, obtaining vertex-wise cortical thickness,

surface area and gyrification LGI maps for each brain. Pial surfaces obtained via Freesurfer were then used to calculate ephaptic modulation using the EMOD1 coefficient (Equation 8 with $l_0 = 5mm$). A first average ephaptic map was obtained by averaging the resulting 401 EMOD1 maps (Figure 4A, Figure S4). As expected, following cortical gyrification patterns, the topography of EMOD1 displayed higher values along the sulci walls as well as medial regions such as the precuneus, and anterior cingulate cortex (see figures for statistical results).

In order to understand the relationship between ephaptic and other cortical morphologies (i.e., cortical thickness, surface area, gyrification), vertex-wise correlation was performed between EMOD1 and each morphological metric (Figure 4B). EMOD1 displayed significant but spatially different correlations with all the three morphologies, suggesting the magnitude of ephaptic modulation as potentially resulting from different cortical, non-exclusive structural patterns. EMOD1 also displayed a positive correlation with gyrification and surface area, and a negative correlation with cortical thickness following sulcal patterns (Figure 4B).

2.4 Changes in Ephaptic Modulation with Aging

Vertex-wise correlation between EMOD1 and age produces a bilateral pattern involving primarily sensorimotor regions, insular cortex and anterior cingulate cortex (Figure 5A). The same correlation was performed for thickness, gyrification and surface area. Globally, all metrics show a tendency to decrease with age. The decrease is very well approximated by a linear function for the EMOD1, average LGI and average thickness metrics, with R^2 values of the linear fits of 0.34, 0.36 and 0.44, respectively. All of these fits are statistically significant, with p-values of 3.7×10^{-38}, 6.5×10^{-41} and 9.6×10^{-53}, respectively. For the total cortical area, the fit is worse (R^2 of 0.19) but still statistically significant (p- value of 4.1×10^{-20}). Pearson-correlation coefficients between EMOD1 and average LGI/thickness are also relatively high (0.52 and 0.43, respectively).

3 DISCUSSION

Understanding the functional role of ephaptic mechanisms can, among others, shed new light on the mechanisms underlying neuronal oscillations or help drive the design of better brain stimulation solutions. Research can be guided by focusing on the main features of ephaptic interactions: very fast, bidirectional, propagation of information (see Table S1) between cortical sites, influencing both local and synaptically distant regions as long as they are near in (3D) space, and in a direction dictated by the state and orientation of the emitting and receiving populations (i.e., with effects that can be both excitatory and inhibitory). For example, ephaptic interaction may play an important role in cortical recurrent computation, providing the means for fast integration of information across areas with impact at both low and high frequencies. This may be especially important for gamma synchronization, where timing requirements are stringent (*18*). On the other hand, ephaptic interaction has been shown to enable the generation and propagation of slow waves in brain slices–even after they have been split (*5*). Similarly, SEFs could play a role in inter-hemispheric communication, bypassing corpus callosum connections. Other recent work suggests that they could play a role in the modulation of release of extracellular vesicles (*19*), a newly discovered form of cellular communication.

Relying on biophysical modeling and high-resolution neuroimaging analysis, we have built a first metric of ephaptic interaction in the human brain, characterizing its spatial distribution and its relationship with aging. Below we discuss the implications of ephaptic fields in humans, including their potential relevance for regulating brain oscillatory patterns and cortical excitability, their evolutionary meaning as well as potential role in neurological and pathological disorders.

3.1 Insights from models

Modeling results confirm many of the assumptions of the theoretical predictions. On the one hand, the decay of the electric field created by single dipole sources is confirmed to be well approximated by a $1/r^3$ power law, even in models that consider tissue heterogeneity. In the realistic model, multiple dipole sources create a field that decays slower ($1/r^2$), as predicted by the 3D simplified sulcus model. This confirms that ephaptic interactions are limited to regions that are located close to one another. In the case of sulci, this limits interactions either to the cells close to

the source(s) along the same wall, or cells on the opposite sulcus wall. We note that if the cortical region of interest is undergoing synchronous oscillations in a given band, the ephaptic effects will be in phase for dipoles along the same wall, and antiphase on the opposite wall. In our models with dipole density of 1.0 nAm/mm^2, and assuming that the threshold for interaction was 0.1 V/m, ephaptic effects on the opposite sulcus wall could only be observed in the 3D toy model when the sulcus width was of 1 mm or less, and in the realistic 3D model in portions of the post-central sulcus where its width was the smallest (about 1.4 mm). For comparison, in Chiang et al. (*5*), a separation greater than 0.4 mm in a cut hippocampus slice was sufficient to impede ephaptic wave propagation (see Table 1), which, together with other findings, supports our selection of an analysis threshold of 0.1 V/m.

Further evidence that the scaling of the sources in these models is realistic comes from the observation that the maximum electrostatic potential recorded at scalp level in the realistic head model varied between 16 and 32 μV, respectively for a dipole density of 0.5 and 1.0 nAm/mm^2. Since these dipoles comprise a cortical area of 5.3 cm^2, these results seem consistent with the rule of thumb that ~6 cm^2 of activated cortical area are needed to produce detectable EEG at scalp level (*7*).

3.2 Topography of Ephaptic Fields in the Human Brain

As we have seen, EMOD1 is related to other metrics such as gyrification and cortical thickness. The latter is hardly surprising, since cross-sulcal ephaptic interaction requires the presence of cortical folding. The current study may provide further clues into the importance of gyrification as a zero-order proxy for ephaptic interaction. Studies have indicated that cortical gyrification is strongly and positively related to cortical volume but negatively related to cortical thickness in many regions of the cortex, and that frontal gyrification is positively related to performance in working memory and mental flexibility tasks (*20*, *21*). Such results support the view that greater cortical gyrification is related to bigger brain volumes and better cognitive function. One advantage of gyrification is thought to be increased speed of brain cell communication, since cortical folds allow for cells to be closer to one other, requiring less time and energy to transmit neuronal electrical impulses (*17*). Ephaptic interactions and EMOD1 reflect similar advantages.

From an evolutionary point of view, we may hypothesize that natural selection forces that promoted folding the cortex to fit a larger cortical surface in a more static cranium (i.e., cortical gyrification), as a byproduct made available ephaptic interaction as a form of information transfer, which then also underwent natural selection. Across species, the degree of cortical folding correlates with brain weight and, more specifically, with cortical surface area. In all major mammalian lineages, the species with large brains tend to have more highly folded cortices than species with smaller brains (v. (*22*) and references therein). The pilot whale and bottlenose dolphin display the highest gyrification index values. The human brain, while larger than that of a horse, shows a similar gyrification index. Rodents generally display the lowest gyrification. Nonetheless, some rodents show gyrencephaly and a few primate species are quite lissencephalic. Research on the evolutionary biology studying ephaptic transmission is deeply needed.

3.3 Ephaptic Fields and Age

Analysis of the metrics computed on the MRI dataset indicate a robust correlation of EMOD1, cortical thickness, LGI, and surface area with age, as displayed in Figure 5. Not surprisingly, these metrics display moderate inter-correlations stemming from the covariation of cortical folding and sulcal separation. The index proposed here, which stems from physiological considerations related to ephaptic coupling, relies strongly on the notion of sulcal width and dipole strength (cubic) decay with distance. Studies of sulcal widening have shown it is associated to aging, decreased cognitive ability, dementia and schizophrenia (*15*). The negative association observed between EMOD1 and age suggest a highly speculative yet interesting scenario, where the decrease of ephaptic coupling with age may contribute to loss of control over oscillatory patterns and cortical excitability, potentially contributing to age-related cognitive changes. Furthermore, pathologies associated with cortical atrophy, e.g., dementia or traumatic brain injury, would alter ephaptic transmission as well, contributing to the pathophysiology as well as cognitive and behavioral symptoms.

Related to age-related changes in brain structures, the concept of “brain age” has been recently explored by multiple groups, looking at how structural MRI data can be used to estimate the “actual” biological age of a given brain as compared to his chronological age (*23–25*). Such analysis is carried out by fitting a model estimating chronological age by means of structural MRI data in a sample of age matched participants, to then compare residual values for each participant

and label each brain as respectively "older" or "younger" than its reference cohort. Interestingly, estimated brain age has been shown to correlate with mortality, making a very interesting novel health biomarker (*24*). The structural properties such as LGI, thickness and grey matter density are considered, but no studies have investigated the potential role of ephaptic coupling distribution in determining brain age. Together with other potential mechanisms, such as functional reallocation of fMRI connectivity patterns, ephaptic coupling might constitute another key element to determine and maintain brain age.

3.4 Ephaptic role in neurological disorders

Hypersynchronized activity in seizure can generate large rhythmic fields of 20–70 V/m in the hippocampus and 3–9 V/m in the neocortex (v. (*26*)). Interictal discharges generate strong ephaptic perturbations that might very rapidly alter brain dynamics and cause, or at least contribute to, their deleterious effects on brain function and cognition, as also discussed in (*3*). Interestingly, cortical malformations of various types, including shallow sulci and defects of cellular migration, have been described in epilepsy as well (*27*), possibly linking cortical morphology and aberrant epileptic activity through alterations of ephaptic transmission.

More specifically, ephaptic interaction might play a role in the pathogenesis of seizure via its potential contribution to self-regulation of cortical excitability. As the cortical walls come in close proximity due to cortical folding, by projecting activity with the opposite phase on neighboring areas, ephaptic interaction might protect the brain from hypersynchronization. By the same token, the increasing amplitude and spatial extent of electrical activity generated during the last stage of a seizure (see, e.g. (*28*)) may act, through ephaptic interaction, as a homeostatic mechanism to end the seizure. Interestingly, focal cortical dysplasia lesions associated with epileptiform activity are preferentially located at the bottom of abnormally deep sulci (*29*), where such ephaptic homeostatic control would be weakest for geometric reasons.

Alteration of ephaptic interaction can also shed new light on other human brain disorders that are accompanied by change in cortical gyrification. For instance, Lissencephaly is a rare, genetically related brain malformation characterized by the absence of normal convolutions in the cerebral cortex and an abnormally small head. Symptoms may include unusual facial appearance,

difficulty swallowing, failure to thrive, muscle spasms, seizures, and severe psychomotor retardation. Laminar heterotopia is a rare condition consisting in an extra layer of gray matter underlying properly migrated cortex, usually associated with epileptiform activity, cognitive deficits and alterations of functional connectivity patterns (*30*,*31*). Polymicrogyria is a condition in which the brain has an overly convoluted cortex. Symptoms can include seizures, delayed development or weakened muscles. Higher levels of gyrification are also found to relate to greater local connectivity in the brains of individuals with autism spectrum disorders, suggesting ephaptically mediated hyperconnectivity (*32*). The same could be predicted of healthy populations: increased ephaptic coupling (LGI and EMOD) would be associated to increased functionally connectivity, especially at high frequencies. Similarly, the brains of patients with schizophrenia also show reduced cortical thickness and increased gyrification when compared to healthy brains (*33*). Further studies on ephaptic transmission in various pathologies may offer novel insights to account for the identified alterations in brain oscillations and explain cognitive and behavioral symptomatology.

3.5 Relationship of tCS and ephaptic fields

Together with in-vitro and animal work demonstrating the physiological effects of weak electrical perturbations, abundant work in recent years indicates that weak electric fields applied over relatively large areas and over a duration of minutes can have significant physiological after-effects in humans (*34*). Interestingly, as highlighted above ephaptic fields are of the same order of magnitude as those generated by tCS, and both display large correlation scales (of the order of centimeters). In addition, in both types of electric fields are present in the cortex for relatively long times (minutes in tCS and indefinitely in ephaptic fields), and, at the scales of interest, at relatively low frequencies (<< 1 kHz). These similarities suggest that the neuromodulatory effects of tCS may rely on a natural brain interaction mechanism.

For example, it is likely that the effects of tCS, which generates electric fields of the order of 0.1–2 V/m (as predicted by models and verified experimentally (*35*, *36*)) may ultimately be explained by "spatiotemporal coherence" mechanisms, that is, to the augmented impact of weak but spatially extended, temporally coherent (DC or AC) and persistent (minutes) electric fields (*10*, *37*) on neuronal networks in the presence of background noise. Such "array enhanced"

emission and reception features would apply to both exogenous and endogenous fields.

A consequent question is how we can use these insights for better design of tCS protocols. If tCS leverages a natural and physiologically relevant ephaptic mechanism, understanding it in detail should provide valuable inputs for the design of optimized tCS in disorders such as epilepsy, depression or neuropathic pain, where questions remain on where to apply electric fields, for how long and with what temporal waveforms (DC, AC or endogenous, e.g., as derived from EEG), or, perhaps, to help understand what distinguishes treatment responders from non-responders. In particular, the design of tCS protocols should be conceived from the point of view of generating a summation of endogenous and exogeneous fields which the cortex will interact with as an endogenous one. For example, if age or atrophy (e.g., in dementia) predict a reduced impact of ephaptic interactions, would this also suggest a decrease of response to tCS? The hypothesis here would be that a brain that has lost the ability to engage in ephaptic communication will similarly be less sensitive to the effects of exogenous fields.

3.6 Limitations of the study and future directions

The conclusions drawn from our electric field models are subject to uncertainties in some parameters that may affect the volume conduction effects of the currents induced by the dipole sources. Some of these parameters are the conductivity properties of the tissues in the head in the low-frequency range of EEG. These conductivity values are known to considerably influence the electric field distribution in the brain, but the reported range of values in the literature is still somewhat inconsistent (*38*). They are also known to vary with individual anatomy, age and disease (*39–42*). Other important parameters in the model are dipole density and patch size. These are of critical importance, since they influence the location and size of the areas which are influenced by source activity.

Another important limitation in this study is the use of a simplified metric (EMOD1) as opposed to a full calculation of the ephaptic field generated by cortical dipoles (EMOD proper, Eq. 4). This represents a convenient trade-off to be able to evaluate this metric on a large dataset, but it may be improved in the future. In addition, we have used here an interaction model which does not consider the complexity or spatial distribution of pyramidal neurons, or the effects on

other types of neurons, much as it is done in practice, with some justification (*10*, *43*)(*10, 33*), in the analysis of tCS effects. Finally, the effects of tCS have been studied in computational models of the brain (*43–45*) using the lambda-E model discussed above and ignoring the intricacies of cortical network circuitry. This is a simple model that will be improved in the future.

Further work remains to be carried out to disentangle the differential contributions of EMOD1, cortical thickness and other cortical morphologies to explaining measures of brain function and cognition. An interesting line of research will be to determine computationally the impact of ephaptic fields on neuronal dynamics in both the healthy and pathological cortex, along the lines of (*45*).

4 Conclusions

Our findings, in line with earlier experimental work, suggest that ephaptic transmission could constitute the basis of a novel framework for the understanding of brain function and human cognition, as well as neurological and psychiatric pathology where brain structural alterations are present.

5 MATERIALS AND METHODS

5.1 Mechanisms

Given their anatomical characteristics (elongated form factor, which enhances the effects of electric field on membrane polarization), organization (horizontal connectivity, homogeneous orientation in cortical patches and temporal synchrony (*8*)), cortical pyramidal cells are well suited as electric field generators (*8*). In analogy with reciprocity principles that apply to electromagnetic radiation antennae, for the same reason they are good field sensors of quasi-static (endogenous or exogenous) electric fields. Other cortical neuron types, however, may also play a role.

tCS (also known as tES) is a family of noninvasive techniques that include direct current (tDCS), alternating current (tACS), random noise current stimulation (tRNS) or others using specially designed waveforms. It consists in the delivery of weak current waveforms through the scalp (with electrode current intensity to area ratios of about 0.3–5 A/m^2) at low frequencies (0–1 kHz) resulting in weak but spatially extended electric fields in the brain (with amplitudes of about 0.1–2 V/m). tCS is applied during several minutes (typically ~20 minutes). Such electric fields do not initiate *per se* action potentials, but they can influence the likelihood of neuronal firing by the modulation of neuronal transmembrane potentials in relatively large cortical patches, resulting in changes in firing rates and spike timing. The sustained application of such weak fields during sufficiently long periods of time (several minutes) leads to plastic changes of neuronal connectivity through Hebbian mechanisms (see, e.g., (*46–48*)). Thus, like SEFs, the main characteristics of exogenous tCS macroscopic fields are that they are weak, low frequency with moderate to large spatial correlation scales (> 1 cm), and, in practice, applied for relatively long times.

The concurrent effects of tCS are understood to be mediated by the coupling of electric fields to ordered populations of elongated neurons, especially pyramidal cells (see (*10*, *49*) and references therein). Neurons are influenced mostly by the component of the electric field parallel to their trajectory (*2*, *50–53*), and, therefore, knowledge about the orientation of the electric field is crucial to predict the effects of stimulation. The components of the field perpendicular and parallel to the cortical surface are of special importance since pyramidal cells near the cortical surface are mostly aligned perpendicularly to the surface, while many cortical interneurons and axonal projections of pyramidal cells tend to align parallel to the surface (54–56). For a long, straight finite fiber with

space constant λ in a homogeneous electric vector field E, the transmembrane potential difference is largest at the fiber termination, with a value that can be approximated to first order by

$$\delta\Phi = \lambda \boldsymbol{n} \cdot \boldsymbol{E} \equiv \boldsymbol{\lambda} \cdot \boldsymbol{E}, \tag{1}$$

where $\boldsymbol{n}$ is the unit vector defining the fiber axis in the orthodromic direction (see Figure 1). In this approximation, which is sometimes called the "lambda-E model" (10, 57), the spatial scale is provided by the neuron space constant, and the effect is modulated by the relative orientation of field and elongated neuronal populations. The effect is thus determined by both field magnitude and by its direction.

Although membrane perturbations from weak fields are sub-threshold (about 0.1–0.2 mV per V/m applied (*49*)—significantly lower than the 20 mV depolarization required to bring a neuron from resting potential to spike threshold in vitro (*58*))—, nonlinear effects in coupled populations probably lead to an amplification of effects. For example, mathematical models have demonstrated the amplification of weak but coherent signals in networks of nonlinear oscillators (see, e.g., (*49–51*)(*59*, *59*, *60*)) and, more specifically, in computational models of neural circuits (*2*, *3*)). This effect is ultimately dependent on the coupling strength of network elements and their architecture, while noise can contribute to the enhancement of small but homogeneous perturbations in the network (array enhanced stochastic resonance). Thus, co- operative effects arising from noise and coupling in coupled systems can lead to an enhancement of the network response over that of a single element. Such amplification mechanisms could also play a role in other phenomena where a surprising sensitivity to weak perturbations has been found, as with the effects of Earth-strength magnetic field rotations in EEG alpha band activity (*61*).

In summary, assemblies of neurons, if appropriately and homogenously oriented, can function as antennae for ephaptic coupling. We adopt here the lambda-E model to estimate ephaptic effects, given the similar features of exogenous and endogenous fields of interest.

5.2 Estimates of endogenous field strength from reciprocity arguments and EEG

While in the next sections we model SEFs in the cortex using finite element models, here we provide some estimates from reciprocity considerations (*62–64*) by leveraging earlier work modeling the electric fields generated by tCS. Realistic head modeling shows that tCS fields associated to typical 1 mA bipolar transcranial current injection montages are of the order of 0-0.5

V/m (electric field normal to the cortex, E_n) (*65*), and about 5–10 times smaller when averaged over cortical patches at tCS resolution scales (several cm^2). These models have now been validated by invasive measurements (*6*, *35*, *36*), where a bipolar current of about 1 mA leads to median electric field magnitudes of the order of 0.1 V/m.

According to the reciprocity theorem, the magnitude of the E- field normal to the cortical surface induced by a given tCS montage is proportional to the sensitivity of the same montage when used for EEG to monitor the electrical signals generated by a dipole source at the same point in the cortical surface and oriented perpendicularly to it. Let us denote by $V_{ab} = 1\ mA$ the current applied from point a to point b in the scalp that induces the cortically normal electric field E_n somewhere at a point x in the cortex. Consider a hypothetical reciprocal EEG measurement where we observe a potential difference $V_{ab} = 10\ \mu V$ between the same points a and b produced by a dipole located at x and normal to the cortical surface—such as the one in Figure 1. The reciprocity theorem implies that we can replace the pair (E_n, I_{ab}) with (V_{ab}, p) with the ratio of the first pair the same as the ratio of the second. Hence, from the current-electric field data pair we can deduce, given V_{ab}, a value for a reciprocal dipole p: $V_{ab}/p = -E_n/I_{ab}$, which implies $|p| = |I_{ab}V_{ab}/E_n| = 10 \times 10^{-6}\ V \times 10^{-3}\ A/(0.1\ V/m) = 100\ nA \cdot m$ using a value of $E_n \approx 0.1\ V/m$. So, if a lone dipole located at x were responsible for the observed V_{ab}, it would have this strength. As an example, for the chosen realistic head model sulcus model described below (Section 5.4), we calculated the voltage distribution at the scalp induced by such a single 100 nAm source dipole. The dipole was oriented normal to the cortex. At that location, the normal component of the electric field generated by a montage with CP2 as the anode (1 mA) and T10 as the cathode (−1 mA) was of 0.13 V/m. The potential difference between electrodes CP2 and T10 was of 13.1 μV, in agreement with the reciprocity calculation.

Given such a dipole $\boldsymbol{p}$ at location x, what is the associated $\boldsymbol{E}$ at some nearby point y? As a first approximation, the electric field from a current dipole in a homogeneous conductive medium is (in polar coordinates, see (*64*), p. 33):

$$\boldsymbol{E} = -\boldsymbol{\nabla}\Phi = \frac{1}{4\pi\sigma}\boldsymbol{p}\cdot\boldsymbol{\nabla}\left(\frac{1}{r}\right) = \frac{1}{4\pi\sigma}\frac{p}{r^3}\left(\sin\theta\,\hat{\boldsymbol{\theta}} + 2\cos\theta\,\hat{\boldsymbol{r}}\right), \qquad (2)$$

where r is the distance between x and y, and σ the conductivity of the medium. For example, the field magnitude at 1 mm of distance from the idealized dipole on the contiguous

cortical surface is $E \approx 40\ V/m$ ($\theta = 0, \sigma = 0.40\ S/m$ in grey matter tissue, see for instance (*66*)). This is at the high end of DC stimulation regime experiments (in-vitro, see Table 2). At 1 cm distance from the dipole, $E = 0.05\ V/m$. Out in the CSF, where ($\theta = 90, \sigma = 1.79\ S/m$), the magnitudes are $E \approx 4$ and $0.004\ V/m$, respectively. The dipole approximation is applicable for distances significantly larger than the dipole size (the space constant of pyramidal neurons is typically much less than 1 mm, see e.g. (*67*)).

Of course, EEG signals are not generated by single point dipoles but by the summation of fields from extended sources (coherent patches) and collections of them. Despite of this, to the extent that these sources are small compared to scales we are interested in, these estimates give an order of magnitude of what we may expect to observe. Measurements in the human neocortex indicate that current dipole surface densities in the cortex are in the range of $0.16 - 0.77\ nA \cdot m/mm^2$ (*16*, *17*). There appears to be a maximum value across brain structures and species ($1 - 2\ nA \cdot m/mm^2$). Studies using combined electrocorticography and MEG show that coherent area sizes of the order of 1 to 20 cm^2 are needed for MEG detection, with the larger ones observed in epileptic discharges (*68*). At a density of $0.25\ nA \cdot m/mm^2$, our hypothetical dipole of $100\ nA \cdot m$ above would be realized over a patch of about $4\ cm^2$.

Finally, we note that cortical folds bring together pyramidal populations of opposite orientation to distances of much less than $1\ cm$ (even submillimeter) which should play an important role in extending the effects of dipole fields beyond their immediate neighborhoods.

5.3 Simplified 3D volume conductor model of ephaptic interactions

To investigate in more detail the electric field distribution created by dipole sources on a heterogeneous volume conductor, we first created a 3D finite element toy model. The model, shown in Figure 2, includes a simplified representation of a sulcus and of the scalp, skull, cerebrospinal fluid (CSF), grey- matter (GM) and white-matter (WM) tissues. This geometry was then extruded $100\ mm$ along the z-axis (out of plane direction). Sources were placed in a patch located in the posterior wall of the sulcus, in the GM-CSF interface.

The tissues were assumed to be homogeneous and isotropic, with electrical conductivity

values appropriate to the low frequency range of interest (*65*, *66*): $0.33, 0.008, 1.79, 0.40$ and $0.15\ S/m$ respectively for scalp, skull, CSF, GM and WM. Sources were modeled as point dipoles, with a direction perpendicular to the sulcus wall. Two models for the sources were built: a single dipole model and a multiple dipole model (77 dipoles located in a $1\ mm \times 1\ mm$ regular grid comprising a $60\ mm^2$ patch — as shown in Figure 2). The single dipole model was used to study the electric field distribution of a dipole source and its decay with distance. The multiple dipole model was used as a more realistic representation of a patch of sources. For each source model, the sulcus width was varied between 1 and 3 mm, which are median sulcus width values on the low/high-end of the reported sulci width for subjects between 20 and 80 years of age (*15*). All models were solved in Comsol with the AC/DC package (v5.3a, www.comsol.com). The finite element mesh comprised tetrahedral second order Lagrange elements with a minimum size in the GM and CSF layers of 0.5 mm. Dipole sources were modeled with Comsol's "Electric Point Dipole" boundary condition, which allows the user to specify the direction and strength of the dipole.

5.4 Building a realistic brain model of ephaptic fields

The electric fields generated in the brain with tCS can now be readily modeled at the individual level using imaging data (see (*57*, *69*) for recent reviews). We employ here the same techniques to model endogenous fields from cortical dipoles, that is, finite element modeling derived from MRI (see Figure 3). The model, described in detail in (*65*), is based on the Colin27 MRI dataset (http://www. bic.mni.mcgill.ca/ServicesAtlases/Colin27). It includes realistic representations of the scalp, skull, CSF (including ventricles), GM and WM. Each tissue was modeled as explained in the previous section. Dipole sources were placed in the grey matter-cerebrospinal fluid (GM-CSF) surface of the model, perpendicularly to it, in similar fashion to what was done in the 3D simplified model. As before, two source distributions were calculated: a single node source mode and a multiple source model comprising a cortical surface of 5.30 cm^2. In the single source model, the cortical surface was parcellated into 112 AAL areas and a point was chosen randomly in each area, for a total of 112 single source models. The multiple source model was built by placing 133 dipole nodes in the posterior wall of the post-central sulcus (see Figure 3 b). All electric field calculations were performed in *Comsol* with the AC/DC package.

5.5 Ephaptic modulation index (EMOD and EMOD1)

In this section we define an index to estimate, for a given individual brain model, the role of ephaptic modulation. The index provides an average over the cortex of the impact that emitting dipoles have on receivers. We have considered several aspects to define it meaningfully. First, it should reflect the basic physics of dipoles (field decay with distance) and coupling to neurons (directional lambda-E model (*10*)). Second, it should be insensitive to local effects of a dipole on its local neighbors on the cortical manifold, as this will be a strong but unspecific effect. Rather, it should emphasize the effects of neighboring dipoles across-sulcus. Finally, for ephaptic effects from near dipoles to add to some relevant value, they should be *coherent* in time. This means the metric should disregard remote sources (e.g., a few cm away), which will be presumably less coherent. The coherence space scale in the cortex depends on the frequency of the dynamics of interest. For instance, the spatial correlation length of dipole activity in the cortex is larger at lower frequencies. It is often stated that a coherent patch of 6 cm^2 is needed to create signals that can be detected by EEG (*7*). It is for these reasons that EEG power is weaker at high frequencies (there is no frequency dependence on conductivity at the frequencies of interest, as discussed in (*70*)). This also indicates that ephaptic effects are probably frequency dependent, and stronger at low frequencies.

Now, using the lambda-E tCS interaction model, the ephaptic impact of a source dipole at y on a neuron or neuron population receiver at x (in μV) may be approximated by $\varepsilon_y(x) = \boldsymbol{\lambda_x} \cdot \boldsymbol{E_y}(x)$, where $\boldsymbol{E_y}(x)$ is the endogenous electric field vector at x generated by a dipole at y and $\boldsymbol{\lambda_x}$ the space constant vector of the receiver neuron or neuronal population at x. The membrane perturbation may be positive (depolarizing) or negative (hyperpolarizing).

We sum ephaptic the contributions from dipole generators over the cortical mesh surface (all $y \neq x$) *to* produce a total ephaptic impact factor for each cortical location x is (in μV),

$$\varepsilon(x) = \sum_{y \neq x} W(x, y)\varepsilon_y(x) \tag{3}$$

where $W\ (x, y)$ is a support function to account for the requirements of non-local but coherent (not too far) contributions. This is a local measure on the cortical surface, which we can use to produce cortical surface maps of ephaptic effects.

In the same vein, the average global index equation for a cortex is simply (μV):

$$\varepsilon^g = \frac{1}{N}\sum_x \varepsilon(x) = \frac{1}{N}\sum_x \sum_{y \neq x} W(x, y)\varepsilon_y(x) \tag{4}$$

with N the number of nodes in the cortical mesh.

While Equation 4 provides a generic, precise expression (EMOD), it may be hard to compute in practice (a realistic head model of cortical dipole electric field at each node needs to be evaluated). We may approximate it using Equation 2 for very short distances and mutually opposed emitter/receiver dipoles (with $\theta = 0$) as

$$\varepsilon_y(x) = \boldsymbol{\lambda}_x \cdot \boldsymbol{E}_y(x) \approx \frac{2}{4\pi\sigma}\frac{\boldsymbol{\lambda}_x \cdot \boldsymbol{p}_y}{r^3} \tag{5}$$

We will set $\boldsymbol{p}_y = p_0 \delta A \boldsymbol{n}_y$ with $p_0 = 0.5nA \cdot m/mm^2$ and $\boldsymbol{\lambda}_x = \lambda_0 \boldsymbol{n}_x$ with $\lambda_0 = 1mm$. We denote the local unit normal vector at the source at y by $\boldsymbol{n}_y$. We collect some of these factors into a constant for use below, $\kappa = \lambda_0 p_0/(2\pi\sigma)$ (with conductivity evaluated at GM). Based on this, we provide a simplified approximation which uses the fact that dipole strength falls, approximately, as the cube of the distance, with $\boldsymbol{n}_x$ and $\boldsymbol{n}_y$ denoting local unit cortical surface normal vectors at source and receiver locations,

$$\varepsilon(x) \approx -\kappa \sum_{y \neq x} W(x, y)\frac{\boldsymbol{n}_x \cdot \boldsymbol{n}_y}{r^3}\delta A \tag{6}$$

This index takes into account orientation of dipole and affected populations, and in particular, if the effect of the dipole on other regions is excitatory or inhibition. Finally, to select contributions from near dipoles in Euclidean space but geodesically distant on the surface (e.g., across sulci with opposed orientation), we write

$$\varepsilon_1(x) \approx -\kappa \sum_{y \neq x} \Theta[-\boldsymbol{n}_x \cdot \boldsymbol{n}_y]\Theta[l_0 - r]\frac{\boldsymbol{n}_x \cdot \boldsymbol{n}_y}{r^3}\delta A \tag{7}$$

and

$$\varepsilon_1^g \approx -\frac{\kappa}{N}\sum_{x}\sum_{y \neq x} \Theta[-\boldsymbol{n}_x \cdot \boldsymbol{n}_y]\Theta[l_0 - r]\frac{\boldsymbol{n}_x \cdot \boldsymbol{n}_y}{r^3}\delta A \tag{8}$$

that is, with the weighting term $W\ (x, y) = \Theta[-\boldsymbol{n}_x \cdot \boldsymbol{n}_y]\Theta[l_0 - r]$, with $\Theta[x]$ the Heaviside step function (defined as $\Theta[x]$ for $x \leq 0$ and 1 otherwise) and l_0 a scale relevant for interaction (maximal distance to consider coherent contributions). We set $l_0 = 5\ mm$.

We call this simplified index EMOD1 (see Supplementary Materials for a discussion on variants of EMOD1). It can be computed vertex-wise to produce cortical maps or averaged over the surface. Its calculation requires only the segmentation of the cortical surface and calculation of surface normal vectors from MRI images.

5.6 Imaging data and analysis

To test the variation of the ephaptic modulation index with age, we calculated it (using the simplified expression in Equations 7 and 8) for 401 subjects with ages between 16–83 years using a publicly available database. High-quality structural T1-weighted MRIs (3T) were acquired for 401 subjects from the NKI-Rockland database (*71*). MRI images were acquired using a 3-T Siemens MAGNETOM TrioTim with the following parameters: MPRAGE sequence, TR = 1900ms, TE =2.52ms, and TI=900ms, Flip Angle=9 degrees, FOV=250x250mm, voxel size=1 mm isotropic.

Structural T1-weighted MRIs were processed using the Freesurfer v6.0 software package to create three-dimensional representations of cortical surface (*72*). The Freesurfer pipeline includes automated Talairach transformation, segmentation of subcortical white matter and deep grey matter structures based on intensity and neighbor constraints, intensity normalization, tessellation of grey matter-white matter boundary and grey matter-CSF boundary, automated topology correction and reconstruction of cortical surface meshes (*73*). Next, reconstructed white surfaces were registered to Freesurfer template (*fsaverage*) based on cortical folding patterns using spherical

registration implemented in Freesurfer (*mri surf2surf*).

For each subject, we also have computed cortical morphometrics including cortical thickness, surface area, and gyrification. Gyrification quantifies the cortical surface hidden in the sulci as compared to the visible cortical surface. The vertex-wise cortical gyrification was measured by calculating the gyrification index in circular three- dimensional regions of interest (*74*). This method uses an outer smooth surface tightly wrapping the pial surface and computes the ratio between areas of circular regions on the outer surface and their corresponding circular patches on the pial surface (see https://surfer. nmr.mgh.harvard.edu/fswiki/LGI for a description of how to calculate it with Freesurfer). At each vertex, cortical thickness was measured as the distance between white and pial surfaces, and cortical surface area was calculated by averaging the area of all faces that meet at a given vertex on the white matter surface.

Spherical registration implemented in Freesurfer (mri surf2surf) was used to register white matter surfaces into *Freesurfer* common template (*fsaverage*) to perform group-level analyses. We used 10 mm full-width-at-half-maximum (FWHM) Gaussian kernel to smooth cortical thickness, surface area, gyrification and EMOD1 maps.

5.7 EMOD calculation

For EMOD1 calculation, the GM meshes obtained from Freesurfer were corrected from morphological defects using the *Mayavi* (https://docs.enthought.com/mayavi/mayavi/) and *Pymeshfix* (https://pypi.org/project/pymeshfix/) toolboxes for *Python*. Surface normal vectors were then calculated in Matlab (v2018a, www.matlab.com) using the Iso2Mesh pipeline (http://iso2mesh.sourceforge.net/cgi-bin/index.cgi). For each mesh point of the surface we also calculated the Euclidean distances to all the other points in the mesh, and used this information to compute EMOD1 locally and then globally using Equations 7 and 8.

5.8 Statistical Analysis

Statistical analysis of correlations of metrics with age has been carried out using the Pearson correlation coefficient and its associated statistical significance using the Student's t-distribution.

All regressions were performed with the *Statsmodels* package for Python (*75*).

We performed vertex-wise Pearson's correlation analyses between EMOD1 and cortical morphologies (cortical thickness, surface area and gyrification) as well as subjects' age. False discovery rate (FDR) approach was used to control for multiple comparisons (Benjamini-Hochberg procedure, corrected p-value < 0.05) (*76*).

Acknowledgements/Conflict of Interest

Giulio Ruffini is co-founder of Neuroelectrics; Ricardo Salvador and Roser Sanchez-Todo work at Neuroelectrics, a company that produces EEG and tCS systems. Giulio Ruffini would like to thank Niels Birbaumer for inspiring discussions on the relation of tCS with EEG neurofeedback. GR is partially supported by the European FET Open project Luminous (European Union's Horizon 2020 research and innovation programme under grant agreement No 686764). Dr. Pascual-Leone and Dr. Santarnecchi are partially supported by Office of the Director of National Intelligence (ODNI), Intelligence Advanced Research Projects Activity (IARPA), via 2014-13121700007. The views and conclusions contained herein are those of the authors and should not be interpreted as necessarily representing the official policies or endorsements, either expressed or implied, of the ODNI, IARPA, or the U.S. Government. Pascual-Leone is further supported by the Berenson-Allen Foundation, the Sidney R. Baer Jr. Foundation, grants from the National Institutes of Health (R01HD069776, R01NS073601, R21 MH099196, R21 NS082870, R21 NS085491, R21 HD07616), and Harvard Catalyst | The Harvard Clinical and Translational Science Center (NCRR and the NCATS NIH, UL1 RR025758). Dr. Santarnecchi is supported by the Beth Israel Deaconess Medical Center (BIDMC) via the Chief Academic Officer (CAO) Award 2017, the Defence Advanced Research Projects Agency (DARPA) via HR001117S0030, and the NIH (P01 AG031720-06A1, R01 MH117063-01, R01 AG060981-01). The content of this paper is solely the responsibility of the authors and does not necessarily represent the official views of Harvard University and its affiliated academic health care centres, the National Institutes of Health, the Sidney R. Baer Jr. Foundation.

References

1. J. G. Jefferys, Nonsynaptic modulation of neuronal activity in the brain: electric currents and extracellular ions. *Physiol Rev*. **75**, 689–723 (1995).
2. F. Fröhlich, D. A. McCormick, Endogenous Electric Fields May Guide Neocortical Network Activity. *Neuron*. **67**, 129–143 (2010).
3. M. Zhang *et al.*, Propagation of epileptiform activity can be independent of synaptic transmission, gap junctions, or diffusion and is consistent with electrical field transmission. *J. Neurosci.* **34**, 1409–1419 (2014).
4. C. Qiu, R. S. Shivacharan, M. Z. M, D. M. Durand, Can neural activity propagate by endogenous electrical field? *J. Neurosci.* **35**, 15800–15811 (2015).
5. C.-C. Chiang, R. S. Shivacharan, X. Wei, L. E. Gonzalez-Reyes, D. M. Durand, Slow periodic activity in the longitudinal hippocampal slice can self-propagate non-synaptically by a mechanism consistent with ephaptic coupling. *The Journal of Physiology*. **597** (2019).
6. M. R. Krause, P. G. Vieira, B. A. Csorba, P. K. Pilly, C. C. Pack, Transcranial alternating current stimulation entrains single-neuron activity in the primate brain. *PNAS* (2019).
7. P. Nunez, R. Srinivasan, *Electric fields of the brain: the neurophysics of EEG.* (New York: Oxford University Press, 2006).
8. G. Buzsáki, C. A. Anastassiou, C. Koch, The origin of extracellular fields and currents — EEG, ECoG, LFP and spikes. *Nature Reviews Neuroscience*. **13**, 407 (2012).
9. J. D. Jackson, *Classical Electrodynamics* (J. Wiley and Sons, 1962).
10. G. Ruffini *et al.*, Transcranial Current Brain Stimulation (tCS): Models and Technologies. *IEEE Transactions on Neural Systems and Rehabilitation Engineering*. **21**, 333–345 (2013).
11. J. M. McNally, R. W. McCarley, Gamma band oscillations: a key to understanding schizophrenia symptoms and neural circuit abnormalities. *Curr Opin Psychiatry*. **29**, 202–210 (2016).
12. P. B. Fitzgerald, et al, A comprehensive review of the effects of rTMS on motor cortical excitability and inhibition. *Clinical Neurophysiology*. **117**, 2584–2596 (2006).
13. R. Cassani, M. Estarellas, R. San-Martin, F. J. Fraga, T. H. Falk, Systematic Review on Resting-State EEG for Alzheimer's Disease Diagnosis and Progression Assessment. *Disease Markers* (2018), , doi:10.1155/2018/5174815.
14. N. Jackson, S. R. Cole, B. Voytek, N. C. Swann, *eNeuro*, in press, doi:10.1523/ENEURO.0151-19.2019.
15. C. R. Madan, Robust estimation of sulcal morphology. *bioRxiv* (2019), doi:10.1101/452789.
16. S. Murakami, Y. Okada, Invariance in current dipole moment density across brain structures and species: Physiological constraint for neuroimaging. *Neuroimage*. **111** (2015).
17. R. Hari, A. Puce, *MEG–EEG primer* (Oxford U. Press, 2017).
18. G. Buzsaki, *Rhythms of the Brain* (Oxford University Press Press, 2006).
19. Y. Wang, R. Melvin, L. T. Bemis, G. A. Worrel, H.-L. Want, Programmable Modulation for Extracellular Vesicles. *BioRxiv* (2019).
20. P. Gautam, K. J. Anstey, W. Wen, P. S. Sachdev, N. Cherbuin, Cortical gyrification and its relationships with cortical volume, cortical thickness, and cognitive performance in healthy mid-life adults. *Behavioural Brain Research*. **287**, 331–339 (2015).
21. E. Tadayon, A. Pascual-Leone, E. Santarnecchi, Differential Contribution of Cortical Thickness, Surface Area, and Gyrification to Fluid and Crystallized Intelligence. *Cereb Cortex*, doi:10.1093/cercor/bhz082.
22. G. F. Striedter, S. Srinivasan, E. S. Monuki, Cortical Folding: When, Where, How, and Why? *Annu. Rev. Neurosci.* **38**, 291–307 (2015).
23. J. H. Cole, K. Franke, Predicting Age Using Neuroimaging: Innovative Brain Ageing Biomarkers. *Trends Neurosci.* **40**, 681–690 (2017).
24. J. H. Cole *et al.*, Brain age predicts mortality. *Mol. Psychiatry*. **23**, 1385–1392 (2018).
25. J. H. Cole, R. E. Marioni, S. E. Harris, I. J. Deary, Brain age and other bodily 'ages': implications for

neuropsychiatry. *Molecular Psychiatry*. **24**, 266 (2019).

26. J. G. Jefferys, R. D. Traub, M. A. Whittington, Neuronal networks for induced "40 Hz" rhythms. *Trends Neurosci*. **19**, 202–8 (1996).
27. R. J. Leventer, R. Guerrini, W. B. Dobyns, Malformations of cortical development and epilepsy. *Dialogues Clin Neurosci.* **10**, 47–62 (2008).
28. V. K. Jirsa, W. C. Stacey, P. P. Quilichinind, A. I. Ivanov, C. Bernard, On the nature of seizure dynamics. *Brain*. **137**, 2210–2230 (2014).
29. P. Besson, F. Andermann, F. Dubeau, A. Bernasconi, Small Focal Cortical Dysplasia Lesions Are Located at the Bottom of a Deep Sulcus. *Brain*. **131**, 3246–3255 (2008).
30. G. Sprugnoli *et al.*, Functional Connectivity and Genetic Profile of a "Double-Cortex"-Like Malformation. *Front Integr Neurosci*. **12**, 22 (2018).
31. S. Emiliano *et al.*, Cerebro-cerebellar functional connectivity profile of an epilepsy patient with periventricular nodular heterotopia. *Epilepsy Res.* **101**, 280–283 (2012).
32. G. L. Wallace *et al.*, Increased gyrification, but comparable surface area in adolescents with autism spectrum disorders. *Brain*. **136** (2013).
33. L. Palaniyappan, P. Mallikarjun, V. Joseph, T. P. White, P. F. Liddle, *Biological Psychiatry*, in press.
34. M. A. Nitsche, W. Paulus, Excitability changes induced in the human motor cortex by weak transcranial direct current stimulation. *J Physiol*. **527 Pt 3**, 633–9 (2000).
35. A. Opitz *et al.*, Spatiotemporal structure of intracranial electric fields induced by transcranial electric stimulation in humans and nonhuman primates. *Scientific Reports*. **6**, 31236 (2016).
36. Y. Huang *et al.*, Measurements and models of electric fields in the in vivo human brain during transcranial electric stimulation. *eLife*. **6** (2017).
37. G. Ruffini, in *Closed Loop Neuroscience*, A. E. Hady, Ed. (Academic Press, 2016), pp. 241–256.
38. T. Wagner *et al.*, Impact of brain tissue filtering on neurostimulation fields: a modeling study. *NeuroImage*. **85 Pt 3**, 1048–1057 (2014).
39. K. Wendel, J. Väisänen, G. Seemann, J. Hyttinen, J. Malmivuo, The Influence of Age and Skull Conductivity on Surface and Subdermal Bipolar EEG Leads. *Computational Intelligence and Neuroscience*. **2010**, 1–7 (2010).
40. J. Dabek *et al.*, Determination of head conductivity frequency response in vivo with optimized EIT-EEG. *NeuroImage*. **127**, 484–495 (2016).
41. H. Mccann, G. Pisano, Variation in reported human head tissue electrical conductivity values. *bioRxiv*. **511006** (2019), doi:doi: https://doi.org/10.1101/511006.
42. P. C. Miranda, A. Mekonnen, R. Salvador, P. J. Basser, Predicting the electric field distribution in the brain for the treatment of glioblastoma. *Physics in Medicine and Biology* (2014), doi:10.1088/0031-9155/59/15/4137.
43. B. Molaee-Ardekani *et al.*, Effects of transcranial Direct Current Stimulation (tDCS) on cortical activity: A computational modeling study. *Brain Stimulation*. **6**, 25–39 (2013).
44. I. Merlet *et al.*, From Oscillatory Transcranial Current Stimulation to Scalp EEG Changes: A Biophysical and Physiological Modeling Study. *PLoS ONE*. **8**, 1–12 (2013).
45. R. Sanchez-Todo *et al.*, Personalization of hybrid brain models from neuroimaging and electrophysiology data. *BioRxiv* (2018).
46. C. J. Stagg, M. A. Nitsche, Physiological Basis of Transcranial Direct Current Stimulation. *The Neuroscientist*. **1**, 37–53 (2011).
47. J. Modolo, Y. Denoyer, F. Wendling, P. Benquet, Physiological effects of low-magnitude electric fields on brain activity: Advances from in vitro, in vivo and in silico models. *Current Opinion in Biomedical Engineering*. **8**, 38–44 (2018).
48. C. A.Sánchez-León *et al.*, Exploring new transcranial electrical stimulation strategies to modulate brain function in animal models. *Current Opinion in Biomedical Engineering*. **8**, 7–13 (2018).
49. J. Berzhanskaya, N. Chernyy, B. J. Gluckman, S. J. Schiff, G. A. Ascoli, Modulation of hippocampal rhythms by subthreshold electric fields and network topology Modulation of hippocampal rhythms by subthreshold electric fields and network topology. *J Comput Neurosci*. **34**, 369–389 (2013).

50. J. B. Ranck, Which elements are excited in electrical stimulation of the mammalian central nervous system: a review. *Brain Res*. **98**, 417–440 (1975).
51. F. Rattay, Analysis of models for external stimulation of axons. *IEEE Transactions on Biomedical Engineering*. **33**, 974–977 (1986).
52. W. A. H. Rushton, The effect upon the threshold for nervous excitation of the length of nerve exposed, and the angle between current and nerve. *J Physiol*. **63**, 357–77 (1927).
53. M. Bikson *et al.*, Effects of uniform extracellular DC electric fields on excitability in rat hippocampal slices in vitro. *J Physiol*. **557**, 175–90 (2004).
54. B. L. Day *et al.*, Electric and magnetic stimulation of human motor cortex: surface EMG and single motor unit responses. *J. Physiol*. **122**, 449–473 (1989).
55. P. T. Fox *et al.*, Column-based model of electric field excitation of cerebral cortex. *Hum Brain Mapp*. **22**, 1–14 (2004).
56. T. Kammer, M. Vorwerg, B. Herrnberger, Anisotropy in the visual cortex investigated by neuronavigated transcranial magnetic stimulation. *Neuroimage*. **36**, 313–321 (2007).
57. G. Ruffini, F. Wendling, R. Sanchez-Todo, E. Santarnecchi, Targeting brain networks with multichannel transcranial current stimulation (tCS). *Current Opinion in Biomedical Engineering* (2018).
58. A. Liu *et al.*, Immediate neurophysiological effects of transcranial electrical stimulation. *Nature Communications*. **9**, 5092 (2018).
59. M. E. Inchiosa, A. R. Bulsara, Nonlinear dynamic elements with noisy sinusoidal forcing: enhancing response via nonlinear coupling. *Phys. Rev. E*. **52**, 327–339 (1995).
60. J. F. Lindner, et al, Array enhanced stochastic resonance and spatiotemporal synchronization. *Physical Review Letters*. **75**, 3–6 (1995).
61. C. X. Wang *et al.*, Transduction of the Geomagnetic Field as Evidenced from Alpha-band Activity in the Human Brain. *eNeuro*. **ENEURO.0483-18.2019** (2019).
62. H. Helmholtz, Uber einige Gesetz der Vertheilung elektrischer Strdme in korperlichen Leitern, mit Anwendung auf die thierisch- elektrischen Versuche. *Ann. Phys. Chem.* **ser. 3, 29**, 211–233 and 353–377 (1853).
63. S. Rush, D. A. Driscoll, Current distribution in the brain from surface electrodes. *Anesth Analg*. **47**, 717–23 (1968).
64. R. Plonsey, *Bioelectric phenomena* (McGraw-Hill, 1969).
65. P. C. Miranda, A. Mekonnen, R. Salvador, G. Ruffini, The electric field in the cortex during transcranial current stimulation. *Neuroimage*. **70**, 45–58 (2013).
66. N. K. Logothetis, et al, In vivo measurement of cortical impedance spectrum in monkeys: implications for signal propagation. *Neuron*. **55**, 809–823 (2007).
67. A. S. Aberra, A. V. Peterchev, W. M. Grill, Biophysically realistic neuron models for simulation of cortical stimulation. *J. Neural Eng.* **15**, 066023 (2018).
68. M. Oishi *et al.*, Epileptic Spikes: Magnetoencephalography versus Simultaneous Electrocorticography. *Epilepsia*. **43**, 1390–1395 (2002).
69. P. C. Miranda, M. A. Callejón-Leblic, R. Salvador, G. Ruffini, Realistic Modeling of Transcranial Current Stimulation: The Electric Field in the Brain. *Current Opinion in Biomedical Engineering*. **8**, 20–27 (2018).
70. R. Cooper, Comparison of subcortical, cortical and scalp activity using chronically indwelling electrodes in man. *Electroencephalography and Clinical Neurophysiology*. **18**, 217–228 (1965).
71. K. B. Nooner *et al.*, The NKI-Rockland Sample: A Model for Accelerating the Pace of Discovery Science in Psychiatry. *Front Neurosci.* **6** (2012).
72. B. Fischl, FreeSurfer. *Neuroimage*. **62**, 774–781 (2012).
73. A. M. Dale, B. Fisch, M. I. Sereno, Cortical surface-based analysis. I. Segmentation and surface reconstruction. *Neuroimage*. **9**, 179–194 (1999).
74. M. D. Gregory *et al.*, Regional Variations in Brain Gyrification Are Associated with General Cognitive Ability in Humans. *Current Biology*. **26**, 1301–1305 (2016).

75. S. Seabold, J. Perktold, in *9th Python in Science Conference* (2010).
76. Y. Benjamini, Y. Hochberg, Controlling the false discovery rate: a practical and powerful approach to multiple testing. *Journal of the Royal statistical society: series B (Methodological)*. **57**, 289–300 (1995).
77. C. Gabriel, S. Gabriel, E. Corthout, The dielectric properties of biological tissues: I. Literature survey. *Phys Med Biol*. **41**, 2231–49 (1996).
78. J. F. Schenck, The role of magnetic susceptibility in magnetic resonance imaging: MRI magnetic compatibility of the first and second kinds. *Medical Physics*. **815** (1996).
79. C. A. Terzuolo, T. H. Bullock, Measurement of Imposed Voltage Gradient Adequate to Modulate Neuronal Firing. *Proc Natl Acad Sci U S A*. **42**, 687–94 (1956).
80. L. J. Bindman, C. J. Lippold, J. W. T. Redfearn, The action of brief polarizing currents on the cerebral cortex of the rat (I) during current flow and (II) in the production of long-lasting effects. *J. Physiol*. **172**, 369–382 (1964).
81. J. G. Jefferys, Influence of electric fields on the excitability of granule cells in guinea-pig hippocampal slices. *J Physiol*. **319**, 143–52 (1981).
82. S. M. Bawin, A. R. Sheppard, M. D. Mahoney, W. R. Adey, Influences of sinusoidal electric fields on excitability in the rat hippocampal slice. *Brain Res*. **323**, 227–37 (1984).
83. R. S. Ghai, M. Bikson, D. M. Durand, Effects of applied electric fields on low-calcium epileptiform activity in the CA1 region of rat hippocampal slices. *J Neurophysiol*. **84**, 274–80 (2000).
84. J. T. Francis, B. J. Gluckman, S. J. Schiff, Sensitivity of neurons to weak electric fields. *J Neurosci*. **23**, 7255–61 (2003).
85. J. K. Deans, A. D. Powell, J. G. Jefferys, Sensitivity of coherent oscillations in rat hippocampus to AC electric fields. *J Physiol*. **583**, 555–65 (2007).
86. T. Radman, Y. Su, J. H. An, L. C. Parra, M. Bikson, Spike timing amplifies the effect of electric fields on neurons: implications for endogenous field effects. *J Neurosci*. **27**, 3030–6 (2007).
87. C. A. Anastassiou, S. M. Montgomery, M. Barahona, G. Buzsáki, C. Koch, The Effect of Spatially Inhomogeneous Extracellular Electric Fields on Neurons. *J. Neurosci.* **30**, 1925–1936 (2010).
88. S. Ozen *et al.*, Transcranial Electric Stimulation Entrains Cortical Neuronal Populations in Rats. *The Journal of Neuroscience*. **30**, 11476–11485 (2010).
89. D. Reato, A. Rahman, M. Bikson, L. C. Parra, Low-Intensity Electrical Stimulation Affects Network Dynamics by Modulating Population Rate and Spike Timing. *The Journal of Neuroscience*. **30**, 15067–15079 (2010).
90. C. A. Anastassiou, R. Perin, H. Markram, C. Koch, Ephaptic coupling of cortical neurons. *Nature Neuroscience*. **14**, 17–223 (2011).
91. A. Rahman *et al.*, Cellular effects of acute direct current stimulation: somatic and synaptic terminal effects. *J Physiol*. **591**, 2563–2578 (2013).
92. S. L. Schmidt, A. K. Iyengar, A. A. Foulser, M. R. Boyle, F. Fröhlich, Endogenous Cortical Oscillations Constrain Neuromodulation by Weak Electric Fields. *Brain Stimulation*. **7**, 878–89 (2015).
93. M. R. Krause *et al.*, Transcranial Direct Current Stimulation Facilitates Associative Learning and Alters Functional Connectivity in the Primate Brain. *Current Biology*. **27**, 1–11 (2017).
94. M. Vöröslakos *et al.*, Direct effects of transcranial electric stimulation on brain circuits in rats and humans. *Nature Communications*. **9** (2018).
95. B. Asamoah, A. Khatoun, M. M. Laughlin, tACS motor system effects can be caused by transcutaneous stimulation of peripheral nerves. *Nature Communications*. **10** (2019).
96. E. Negahbani *et al.*, Transcranial Alternating Current Stimulation (tACS) Entrains Alpha Oscillations by Preferential Phase Synchronization of Fast-Spiking Cortical Neurons to Stimulation Waveform. *BiorRxiv* (2019).

Table 1: Summary of the maximum values of the scalp electrostatic potential (V) and GM electric field (magnitude, E, and normal component, E_n) induced in all the source distributions used in the realistic head model. For each quantity, two dipole densities are considered: 0.5 and 1.0 nAm/mm^2.

Number of dipole sources	Dipole strength area density ($nA \cdot m/mm^2$)		Individual dipole strength ($nA \cdot m$)		$V_{Scalp}(\mu V)$		Electric field in GM (V/m)			
							E		E_n	
133	0.5	1.0	1.9	3.8	15.9	31.8	8.3	16.7	8.1	16.2
1 (narrow part of the sulcus)	0.5	1.0	2.1	4.2	0.1	0.1	1.6	3.1	1.6	3.1
1 (wide part of the sulcus)	0.5	1.0	2.1	4.2	0.3	0.5	0.3	0.7	0.3	0.7

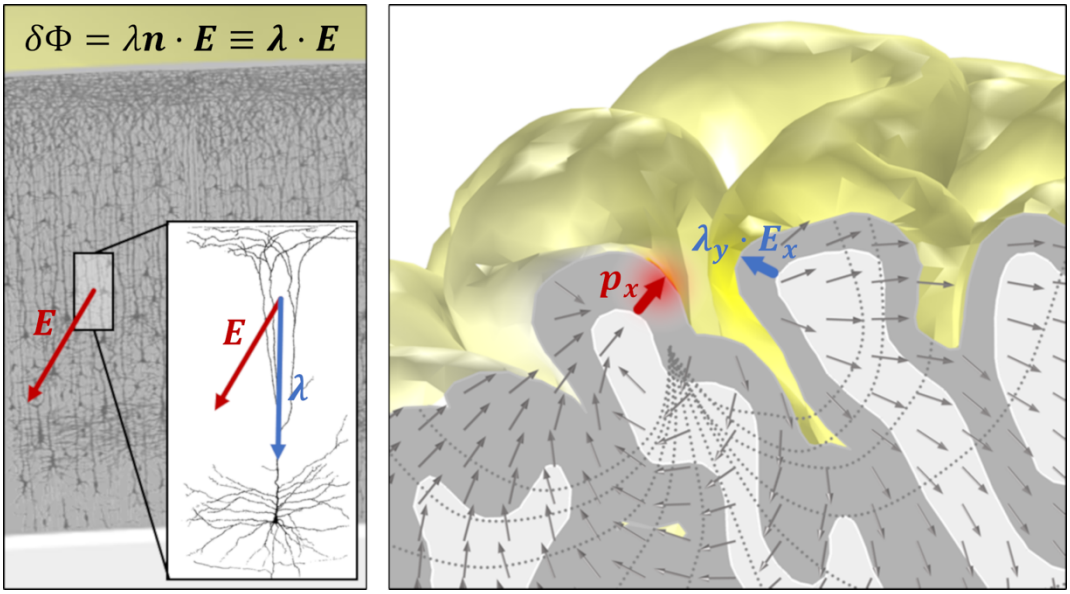

Figure 1: First order model for interaction of electric fields with elongated neurons. On the left, pyramidal neuron population from the human cortex (edited from "Comparative study of the sensory areas of the human cortex" by Santiago Ramon y Cajal, published in 1899, Wikipedia Public Domain). On the right, realistic model of the electric field generated by a current a dipole located at x in the cortex. The orientation of the generating dipole or neuron population and the sensing population (at point y) both play a role.

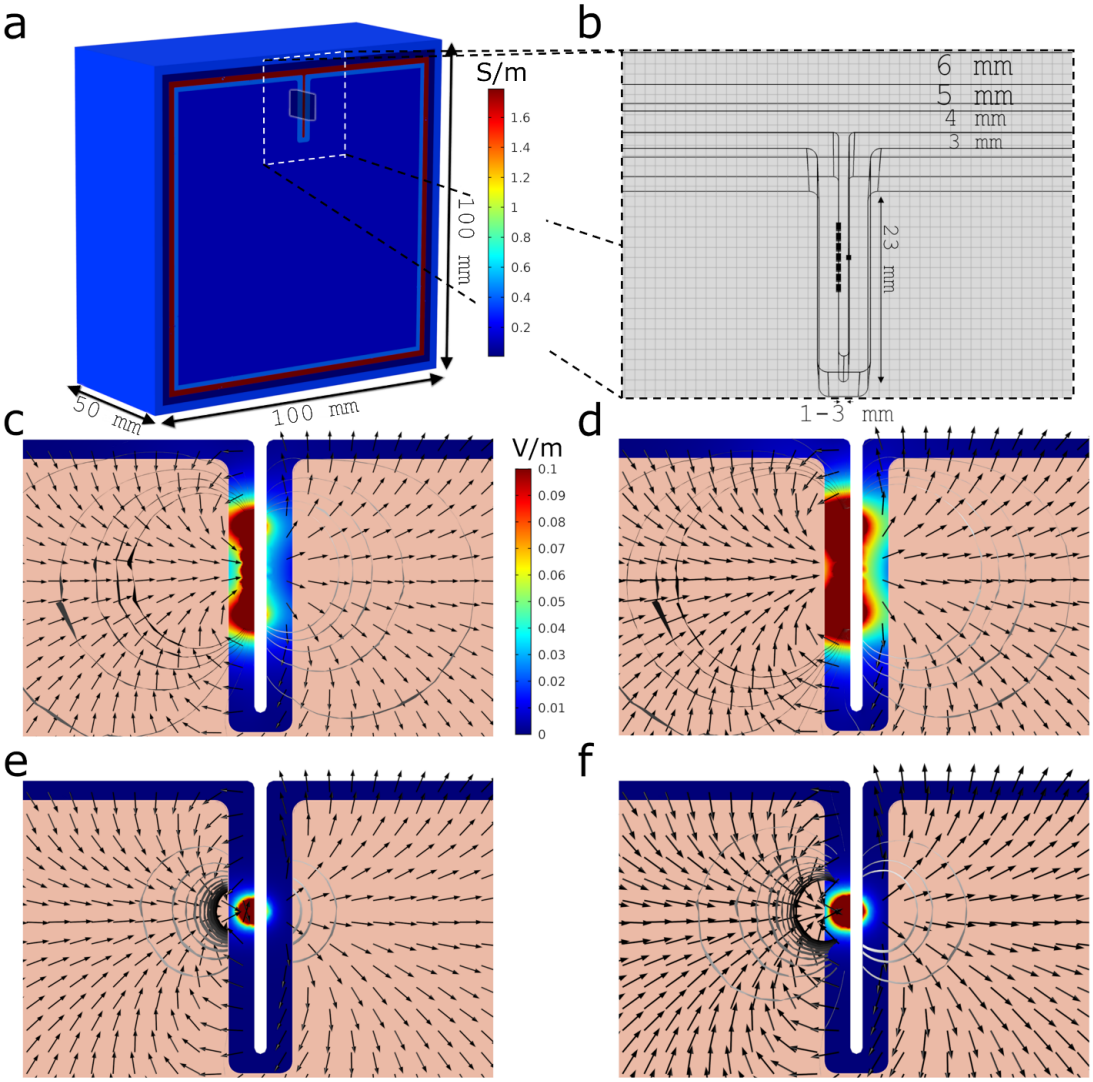

Figure 2: Geometry and electric field distribution in 2D model of a sulcus. (a) 3D view of half of the simplified volume conductor (100×100×100 mm). The different tissues are colored by their respective conductivity, in S/m. The patch of single dipole sources is placed in the central region of the model (posterior wall of the sulcus), covering an area of 60 mm^2. (b) Sagittal view of the model (sulcus width of 1 mm) with dipole sources in its posterior wall. (c-f) Magnitude of the electric field in the GM tissue for models with different source strength and patch distributions (common color scale between plots in V/m). Also shown are vector plots of the electric field and isosurfaces of the electrostatic potential. Left/right columns represent the models with the sources scaled to a density of 0.5 and 1.0 nAm/mm^2 respectively. Top/bottom rows represent multiple/single dipole distributions.

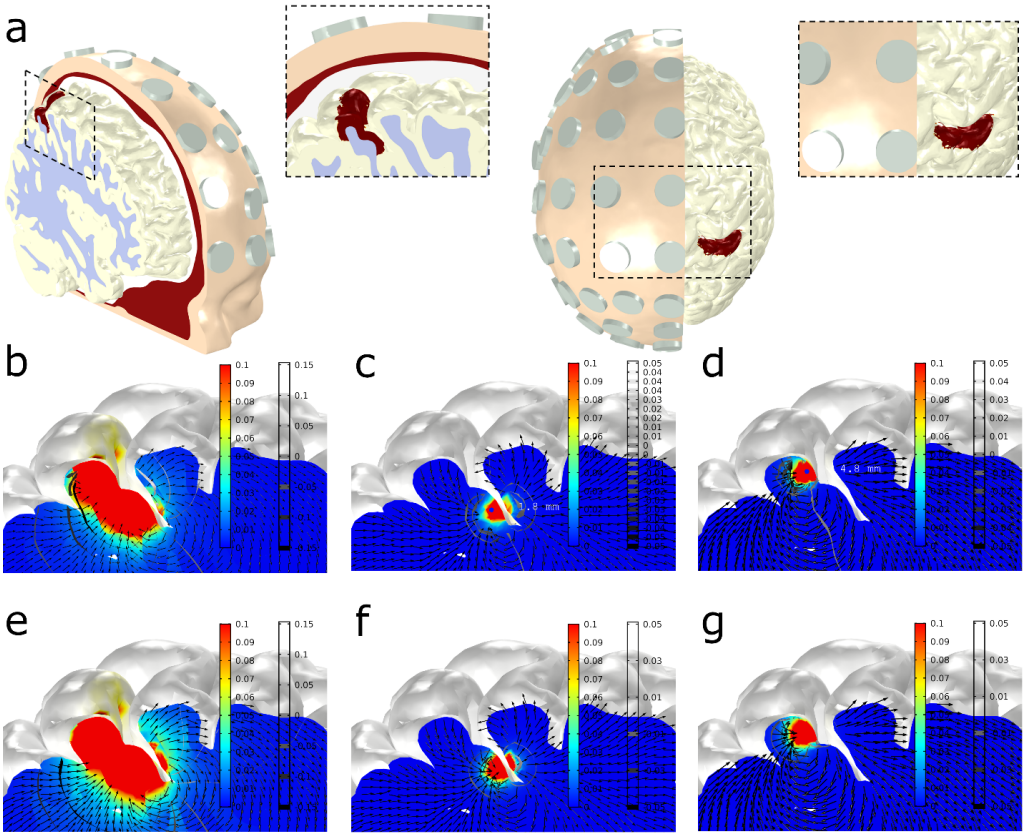

Figure 3: Realistic head model. (a) Two views of the 3D volume conductor geometry, including volumes representing the scalp (yellow), skull (red), CSF (white), GM (grey) and WM (light red). Models of electrodes, placed in the 10-10 EEG positions, are also included in the model (grey). The patch used to place dipoles in the multiple-source model (posterior wall of the post-central sulcus, on the right hemisphere) is displayed in red in the GM volume. It comprises a cortical surface of 5.30 cm^2. The captions provide zoomed views of the cortical patch with the dipole sources. **(b-g):** Electric field magnitude (color bar in V/m) and vector field direction, and isosurfaces of the electrostatic potential (gray-scale, mV) in a sagittal slice passing through the middle of the right hemisphere post-central sulcus. First (b-d) and second (e-f) rows: dipole density per unit area of 0.5/1.0 nAm/mm^2. Columns, from left to right: model with all dipole sources, model with single dipole in narrow region of the sulcus, model with single dipole in wide region of the sulcus. The location of the individual dipoles in the middle and right-most columns are shown as blue circles in figures c and d. The sulcus is approximately 5.5 mm wide in its wide region and 1.8 mm wide in its narrow region.

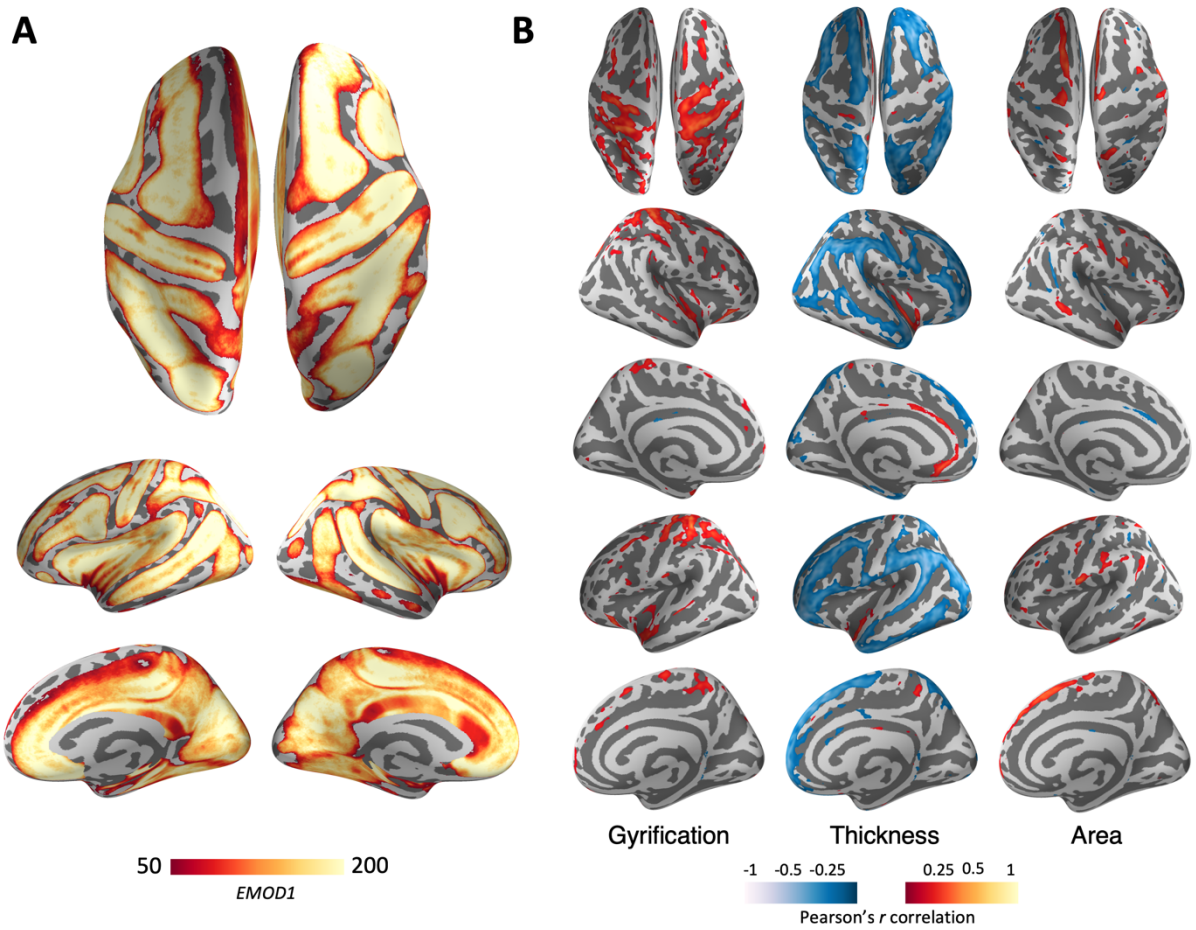

Figure 4: Ephaptic Modulation in the human brain. (A) Average EMOD1. Individual EMOD1 maps are registered to Freesurfer's common template (*fsaverage*) and then averaged at each vertex across subjects. For the purpose of visualization, we have thresholded the average EMOD1 map at EMOD1>50. **(B) Vertex-wise correlation.** At each vertex, the Pearson's correlation coefficient between EMOD1 and cortical surface area, thickness, gyrification and subject's age is computed. The resulting maps are then corrected for multiple comparisons using the Benjamini- Hochberg procedure (p-value <0.05). Pearson's correlation coefficient values for vertices that passed the multiple comparison correction are overlaid on Freesrufer common template (*fsaverage*).

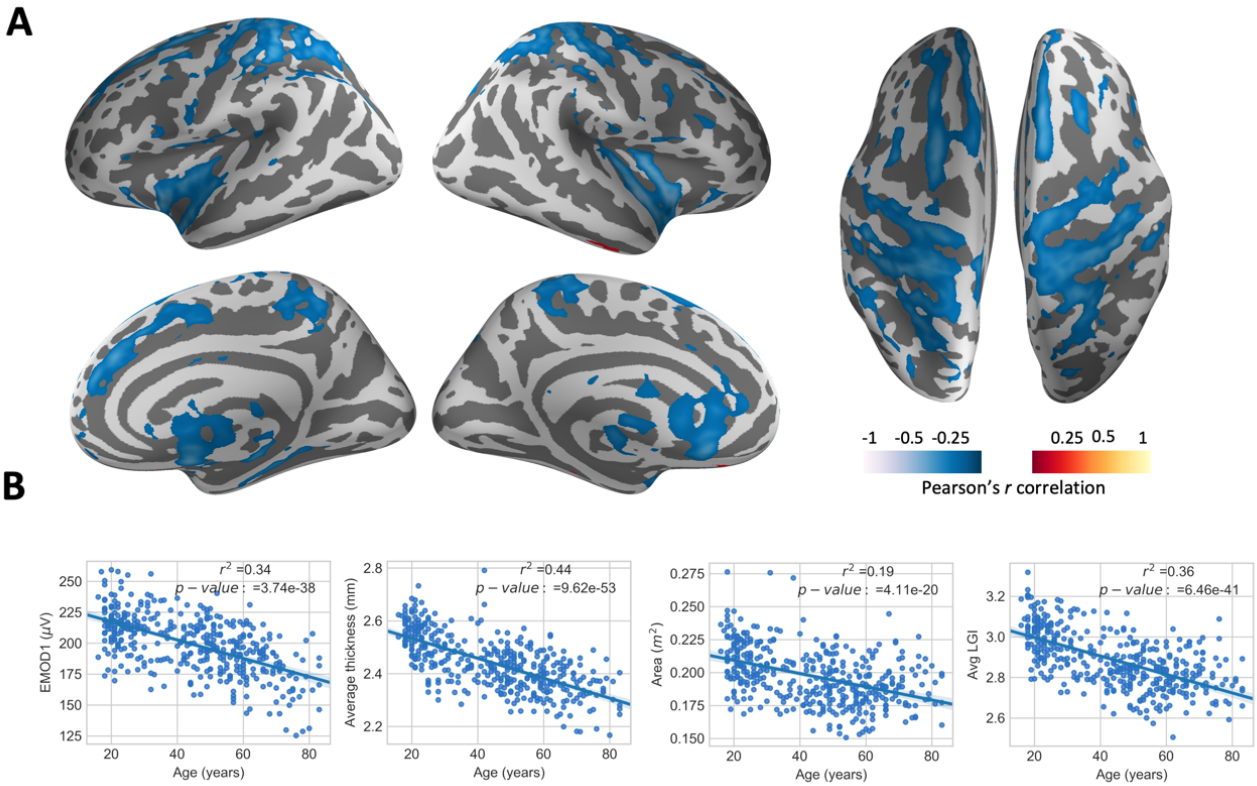

Figure 5. Ephaptic interaction and Aging EMOD1. (A) Vertex-wise EMOD1 values were correlated with age across the sample of 401 subjects, resulting in a weighted map displaying the cortical regions whose ephaptic modulation index is significantly affected by aging. (B) Individual data for correlation between age, EMOD1, as well as cortical morphologies are displayed. Red-yellow shows positive and blue-cyan negative correlations.

SUPPLEMENTARY MATERIALS

Speed of electromagnetic waves in the brain

Table S1 provides a summary of the speed of electromagnetic waves in brain media.

Review of literature on the effects of slow, weak electric fields (SEFs)

See Table S2 for an overview of relevant papers involving weak fields.

Decay of dipole fields

Figure S1 displays plots with the decay of electric field and potential as a function of Euclidean distance for different models.

3D sulcus geometry

Figure S2 displays distance measurements of the sulcus gap.

EMOD1 maps for selected subjects

Figure S3 displays the surface distribution of the EMOD1 coefficient (l0 of 5 mm) for subjects with different ages.

Variants of EMOD1

We provide here some variants of EMOD1. We recall the definition of EMOD1 (with $l0 = 5$ mm):

$$\varepsilon_1^g \approx -\frac{\kappa}{N}\sum_x \sum_{y\neq x} \Theta[-\boldsymbol{n}_x \cdot \boldsymbol{n}_y]\Theta[l_0 - r]\frac{\boldsymbol{n}_x \cdot \boldsymbol{n}_y}{r^3}\delta A \qquad \text{(s1)}$$

The spatial scale l_0 can be varied, but it does not have a big impact on the results.

The first main EMOD1 variant just considers the effect of distance between emitter and receiver, ignoring relative orientation:

$$\varepsilon_0^g \approx \frac{\kappa}{N} \sum_x \sum_{y \neq x} \Theta[l_0 - r] \frac{1}{r^3} \delta A \tag{s2}$$

The second one takes into account relative orientation, but does not enforce the requirement in EMOD1 for opposite orientation of emitter and receiver (which forces cross-sulcal contributions in EMOD1):

$$\varepsilon_{1a}^g \approx \frac{\kappa}{N} \sum_x \sum_{y \neq x} \Theta[l_0 - r] \frac{|\boldsymbol{n}_x \cdot \boldsymbol{n}_y|}{r^3} \delta A \tag{s3}$$

Figure S4 provides linear fits of EMOD variants with age, S5 provides second order fits.

Second order correlations of metrics

Figure S6 provides second order fits of EMOD1, LGI, cortical thickness and area with to age, while figures S7 and S8 provide Pearson cross-correlation between the different metrics.

Scalp map/EEG generated by dipole patch model

Figure S9 displays the scalp map potential for one of the chosen dipole cortical patches (Figure 3, 0.5 nAm/mm^2 density).

Tissue	ε_r	c/v	$v\ (km/s)$	$\tau_{20\ cm}\ (ns)$
Vacuum	1	1	299,792	0.0
CSF	109	10	28,715	0.0
GM	40,699,000	6,380	47	4.3
WM	27,627,000	5,256	57	3.5

Table S1: Relative permittivity, speed of light reduction factor with respect to vacuum (*c/v*), speed of light in tissue (v) in the low frequency range (10 Hz) for various tissues, with data from (77) provided online at http://niremf.ifac.cnr.it/tissprop/. Here we use $v = c/\sqrt{\varepsilon_r \mu_r} \approx c/\sqrt{\varepsilon_r}$ (the relative magnetic permittivity in body tissues is close to unity (78)). The last column is the time in nanoseconds required by ephaptic signals to traverse a sphere of 20 cm. Speed increases 3–4 times at 100 Hz for grey matter (GM) and white matter (WM), and stays constant for cerebrospinal fluid (CSF).

Table S2: Overview of relevant work highlighting the physiological impact of weak electric fields in-vitro or in-vivo and providing quantitative measurements of electric field. The range of electric field magnitude ($E = ||\boldsymbol{E}||$) or of the normal component of the electric field to cell layers (E_n) in V/m (equivalently, mV/mm), that have been shown to influence function are listed. Only references where at least the magnitude of the extracellular electric field is specified are used (the voltage gradient). EPs: evoked potentials. AC: alternating current. DC: direct current. FR: firing rates. LFP: local field potential. SUA/MUA: single/multiple unit activity.

Reference	**Preparation**	$\boldsymbol{E}$	$\lvert\boldsymbol{E_n}\rvert$	**Type**	**Effects**	**Comments**
Terzuolo 1956 (*79*)	Abdominal receptors in the crayfish and cardiac ganglion of the lobster	1–4	1	DC	FR	Fields required were for FR changes were 20 times below threshold. Orientation dependence demonstrated.
Bindman 1964 (*80*)	Rat cortex in-vivo	2.5	2.5	DC	FR and EPs	After effects after 5–10 min stimulation were described.
Jefferys 1981(*81*)	Guinea-pig hippocampus slices	5–70	5–70	DC	EPs	Extracellular currents perpendicular to granule cell layer in hippocampal slices altered their excitability. Effects seen with fields >5V/m.
Bawin 1984 (*82*)	Rat hippocampus slices	2–7	2–7	AC	EPs	Brief stimulation of 5–30 s induced long term changes (more than 10 minutes) of population spike. Exogenous extracellular fields in the tissue were of the order of EEG gradients, suggesting a functional role of EEG-like fields in hippocampus.
Ghai 2000 (*83*)	Rat hippocampus slices	0–8	0–8	DC	Epileptiform activity/LFP	Modulation and full suppression of epileptiform activity was observed at field strengths between 1 and 5 V/m in a direction dependent

Reference	**Preparation**	E	$\lvert E_n \rvert$	**Type**	**Effects**	**Comments**
						manner. Results indicate that DC fields modulate and suppress low-calcium activity by directly polarizing CA1 pyramidal cells.
Francis 2003 (*84*)	Rat hippocampus slices	0.14–3.9 rms value (0.3–6.8 p-p)	same as E	Simulated burst stimulus waveforms with gaussian profile	Entrainment	Neuronal networks respond to fields with more sensitivity than single neurons. Estimated theoretical lower limit for meaningful interaction between electric field and neuron is 0.1 V/m.
Bikson 2004 (*53*)	Rat hippocampal slices	0–200	0–200	DC	Membrane potential, evoked action potentials	The induced polarization was linear (0.12 $\pm$0.05 mV per V/m applied average sensitivity at the soma). DC fields altered the thresholds of action potentials evoked by orthodromic stimulation and shifted their initiation site along the apical dendrites.
Deans 2007 (*85*)	Rat hippocampus slices	0.5–16	0.5–16	DC, AC	FR, Entrainment, Timing, Membrane potential alteration	Decreasing impact w.r.t. DC with increasing frequency. Gamma rhythms modulated by 50 Hz AC with (normal) fields $>$ 0.5V/m (p-p). Effects on both the power spectrum and spike timing depend on AC frequency, with slower frequencies being more effective.
Radman 2007 (*86*)	Rat hippocampal slices	0.5–1.0	0.5-1.0	DC, AC	Timing, entrainment	Spike timing effects are a potential mechanism for the network effects of weak fields.
Fröhlich 2010 (*2*)	Coronal slices of ferret brain	0–4	0–4	DC, AC, in vivo-like	FR, entrainment	Enhancement of slow oscillation at its intrinsic

Reference	**Preparation**	E	$\lvert E_n \rvert$	**Type**	**Effects**	**Comments**
				fields, activity-dependent "feedback" fields		frequency with 2 V/m, entrainment at 0.5 V/m. Significant effect at 0.5 V/m. The E field lines were approximately orthogonal to the cortical surface.
Anastassiou 2010 (*87*)	Rat neocortex slices (layer V pyramidal neurons)	0.7–5.6	N/A	AC (1–9 Hz)	Timing	Ephaptically induced phase locking of spiking is thus more effective, and occurs at lower field strengths, for slow rather than fast modulations of E. E field as small as 0.74 V/m led to entrainment at 1 Hz.
Ozen 2010 (*88*)	In vivo, rat neocortex and hippocampus. Brain slices also analyzed.	1	N/A	AC (0.8–1.7 Hz)	Entrainment	In the intact brain, neurons distant from the stimulation sites can be entrained directly through ephaptic coupling or indirectly, through multisynaptic projections of the directly entrained neurons proximal to the stimulation sites.
Reato 2010 (*89*)	Rat hippocampus slices	0–15	0–15	DC–40 Hz AC	Intracellular Spikes, FRs, spike timing and phase-entrainment resonance	Negative fields decreased the steady-state power of gamma oscillations measured during stimulation, positive fields increased steady-state gamma power. With fields as low as 0.2 V/m phase entrainment can occur with stimulation frequency matched to the endogenous rhythm.
Anastassiou 2011(*90*)	Rat cortical pyramidal neuron slices	0.7–4.2	N/A	AC (1-9 Hz)	Entrainment of spikes, Timing (no FR changes)	Despite small size, fields could entrain action potentials, especially for slow (< 8 Hz) oscillations. LFP like

Reference	**Preparation**	E	$\lvert E_n \rvert$	**Type**	**Effects**	**Comments**
						fluctuations readily entrain membrane potential and spiking.
Berzhanskaya 2013 (*49*)	Rat hippocampal slices	0–60	0–60	DC	Membrane polarization, spike latency and synaptic response	Significant effects on spike latency evoked by somatic current injection. The relative position and spatial orientation of dendritic trees affect both synaptic circuitry and the interaction with electric fields; subthreshold electric fields should robustly alter the balance between different rhythms, and in particular theta-gamma ratio.
Rahman 2013 (*91*)	Rat cortical brain slices	0–8	0–8	DC	field EPSPs	Polarization of both axon terminal and soma are important for effects.
Zhang 2014 (*3*)	Unfolded hippocampus preparation from mice	3–6	N/A	Endogenous fields	Timing	Experiments indicated that longitudinal propagation is independent of chemical or electrical synaptic transmission. Spontaneous epileptiform activity can propagate in both the transverse and longitudinal directions with a speed of 0.1 m/s independently of connectivity.
Schmidt 2015 (*92*)	Mouse neocortical slices	1–2	1–2	AC	FR, Activity spectrum	Weak AC fields enhanced ongoing oscillations only if matched in frequency when strong endogenous activity was present. Enhanced activity occurred at frequency of application when no strong

Reference	**Preparation**	E	$\lvert E_n \rvert$	**Type**	**Effects**	**Comments**
						endogenous activity was present. Results point to the importance of frequency matching when strong endogenous oscillations are present.
Qiu 2015 (*4*)	Rat unfolded hippocampus + compartment model	2–5	2–5	DC	Reduction of propagation speed with blocking field (firing rate changes)	Results show that weak electric fields can be solely responsible for spike propagation at ~0.1 m/s. This phenomenon could be important to explain the slow propagation of epileptic activity or normal propagation at similar speeds.
Krause 2017 (*93*)	Alert nonhuman primates	0.4–0.7	N/A	DC	LFP, SUA/MUA in neocortex	FRs did not change but tDCS induced large low-frequency oscillations in the underlying tissue. Local increase in LFP power near the site of anodal stimulation. More wide-spread effects included a decrease in low-frequency LFP coherence between distant cortical sites along with an increase in high-frequency (gamma-band) coherence.
Voroslakos 2018 (*94*)	Intracellular and extracellular recordings in rats	1–2	N/A	AC	Membrane potential alteration. Firing rate changes. Power in delta band.	Membrane became depolarized or hyperpolarized in a relatively linear manner. Electric fields applied either subcutaneously or transcutaneously which induce at least 1 V/m voltage gradient can affect spiking activity, but stronger fields are needed to

Reference	**Preparation**	E	$\lvert E_n \rvert$	**Type**	**Effects**	**Comments**
						affect network oscillations. NB: Voltage gradients measured parallel to cortex, normal component probably much lower.
Asamoah 2019 (*95*)	Rat motor cortex in-vivo	1	1	1–2.5Hz AC	Single neuron recording entrainment (PLV)	Weak field stimulation (~1 V/m) can entrain neural oscillations (~1 Hz) in the rat motor cortex.
Chiang 2019 (*5*)	Triple-transgenic mice used for longitudinal hippocampal slice studies	5	5	Endogenous fields and anti-fields	Propagating waves	Endogenous electric fields play a significant role in the self-propagation of slow waves (< 1 Hz) in the hippocampus. External anti-fields can block them. Slow activity stopped propagating when cut gap was $> 400\mu$m.
Krause 2019 (*6*)	Alert nonhuman primates	0.2–0.3	N/A	1–100 Hz	Single Neurons in basal ganglia & hippocampus. Spike Timing	tCS consistently influences the timing, but not the rate, of spiking activity. Effects are frequency- and location-specific and can reach deep brain structures; control experiments show that results cannot be explained by sensory stimulation or other indirect influences.
Negahbani 2019 (*96*)	Alert ferrets	<0.5	0.22–0.3	6–14 Hz	Spike-field synchrony	Weak electric fields (< 0.5 mV/mm) comparable to tACS field strength in humans and nonhuman primates can entrain neural spiking in the source of target oscillations.

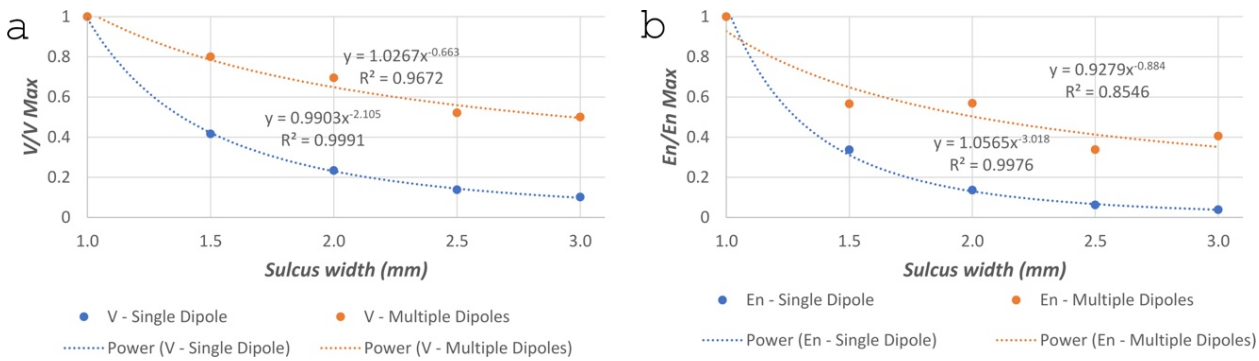

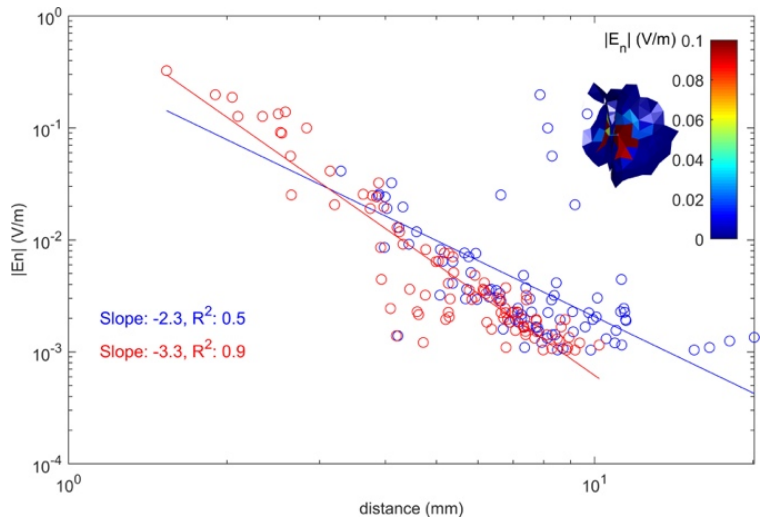

Figure S1: Decay of $\boldsymbol{V}$ and $\boldsymbol{E_n}$ in the 2D and 3D models of the sulcus. Top: field decay in 2D model: (a) Decay of V with sulcus width in the single source model (blue dots) and multiple sources model (orange dots). The fit to a power function is also shown for each model. (b) Same as (a), but now for E_n, the component of the electric field normal to the sulcus wall. Bottom: field decay in 3D model: *loglog* plot of $|E_n|$ (in V/m) in the GM-CSF surface as a function of the logarithm of the geodesic (blue dots) or Euclidean (red dots) distance (in mm) to the dipole. The inset shows E_n (in V/m) in a 3D rendering of the cortical surface. The location of the source is indicated by the red arrow. Only points where the absolute value of E_n is between 0.001 V/m and 1.0 V/m are shown. Linear fits to these plots are also shown, together with the slope and R^2 values.

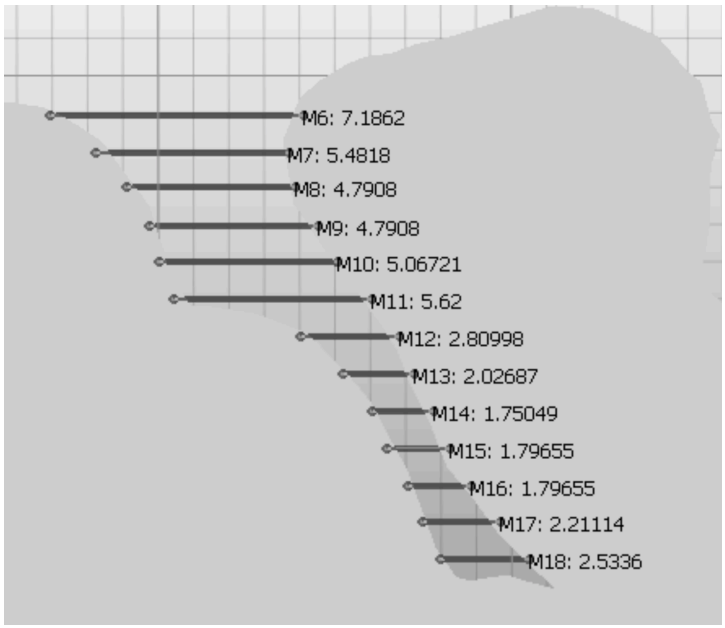

Figure S2: Sulcus geometry Measurements of width (mm) in the sulcus used for realistic modeling in Figure 3 in the main text.

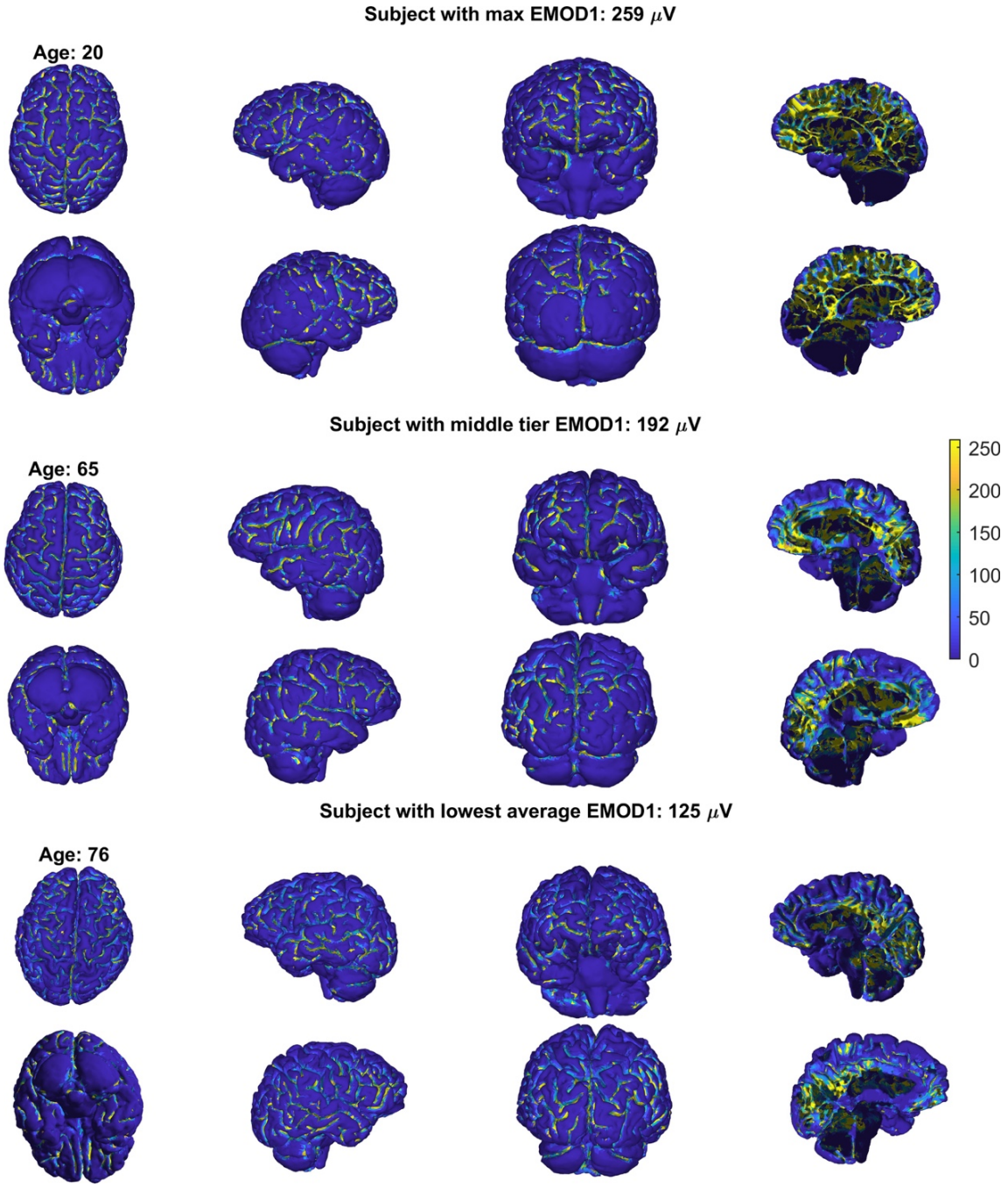

Figure S3: Surface distribution of the EMOD1 coefficient (l_0 of 5 mm) for subjects with different ages. Subjects are presented from highest (top) to lowest EMOD1 (bottom) values. The color scale is common across all the plots. From left-right: top/bottom view, left/right-hemisphere view, front/back view, mid sagittal place left/right hemisphere view.

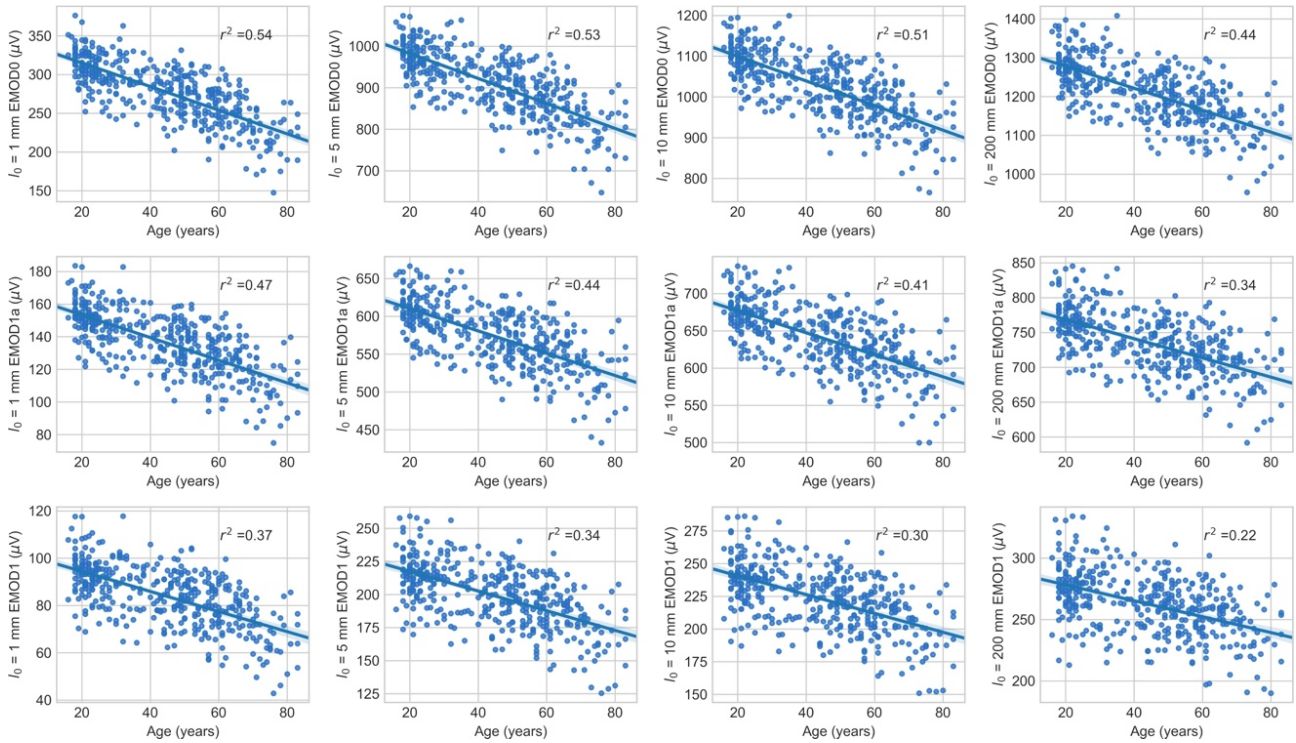

Figure S4: Linear fits of EMOD variants to age. Different rows correspond to different EMOD1 variants: EMOD0 (ε_0^g), EMOD1a (ε_{1a}^g) and EMOD1 (ε_1^g). Different columns correspond to different l0 parameters: 1, 5, 10 and 200 mm, respectively from left to right.

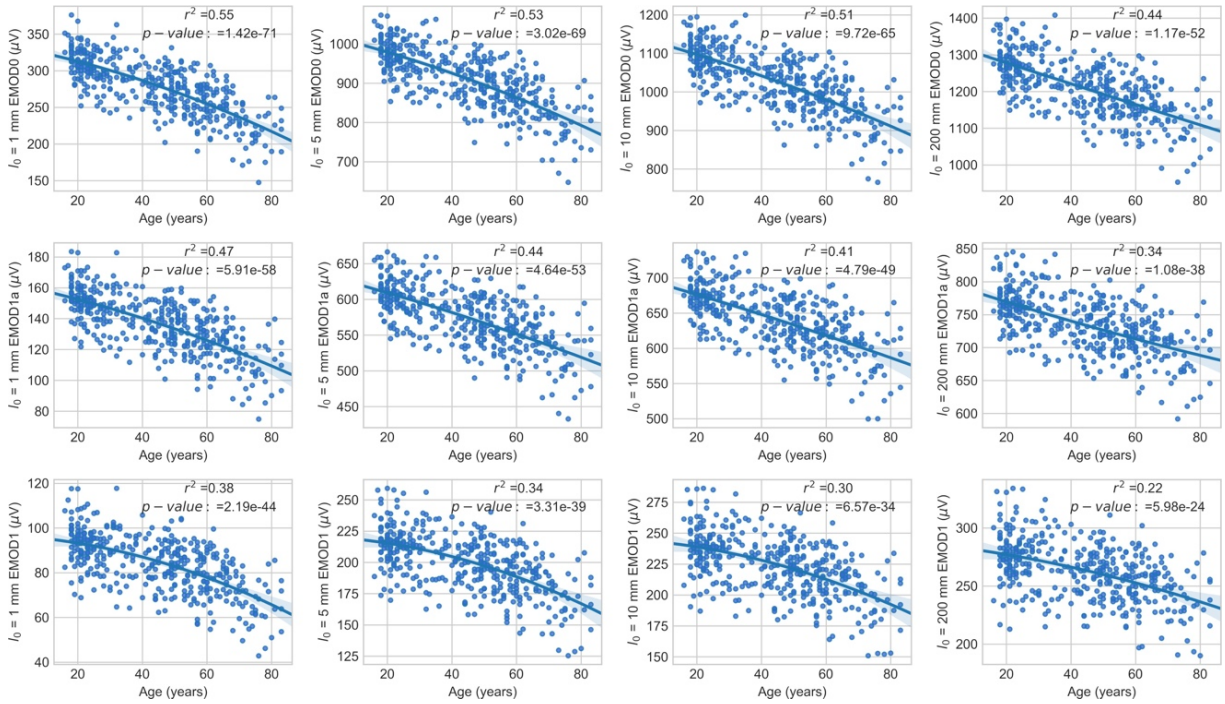

Figure S5: **Second order fits of EMOD variants to age.** Different rows correspond to different EMOD1 variants: EMOD0 (ε_0^g), EMOD1a (ε_{1a}^g) and EMOD1 (ε_1^g). Different columns correspond to different l_0 parameters: 1, 5, 10 and 200 mm, respectively from left to right.

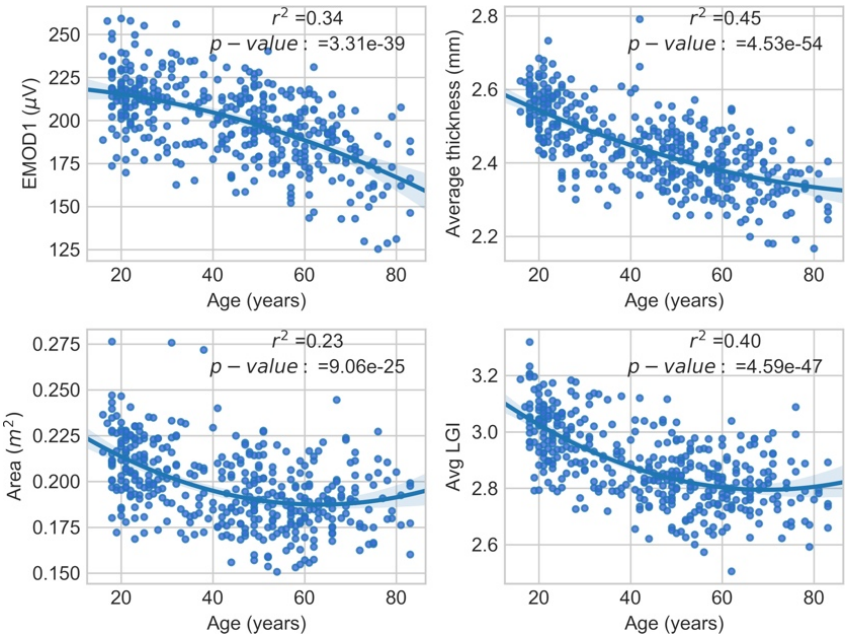

Figure S6: Second order fits of EMOD1, average LGI, average cortical thickness and cortical area to age. For each plot, r-squared and p-values for the fit are shown as well.

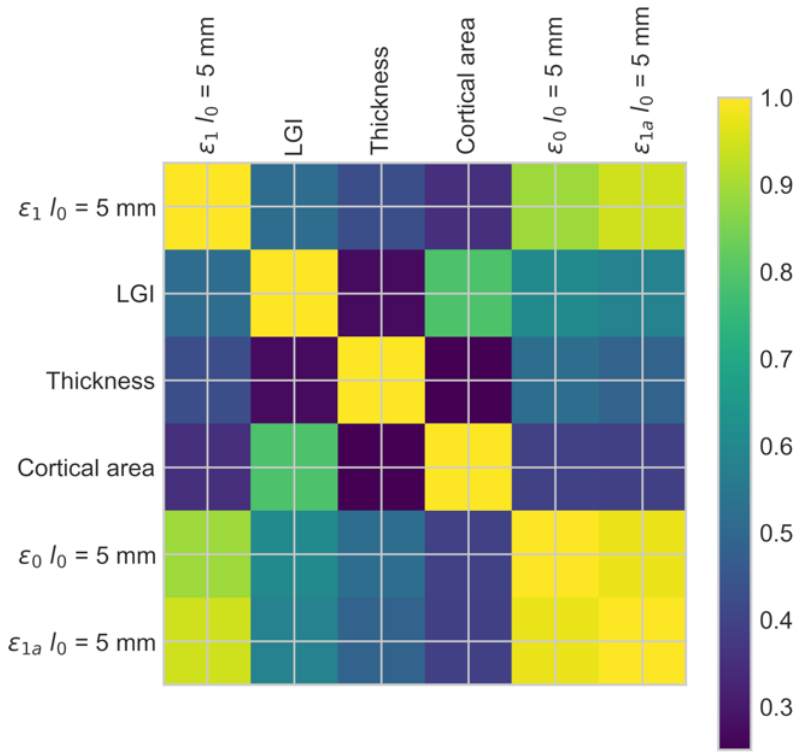

Figure S7: Pearson correlation coefficients between different EMOD variants, average LGI, average cortical thickness and total surface area.

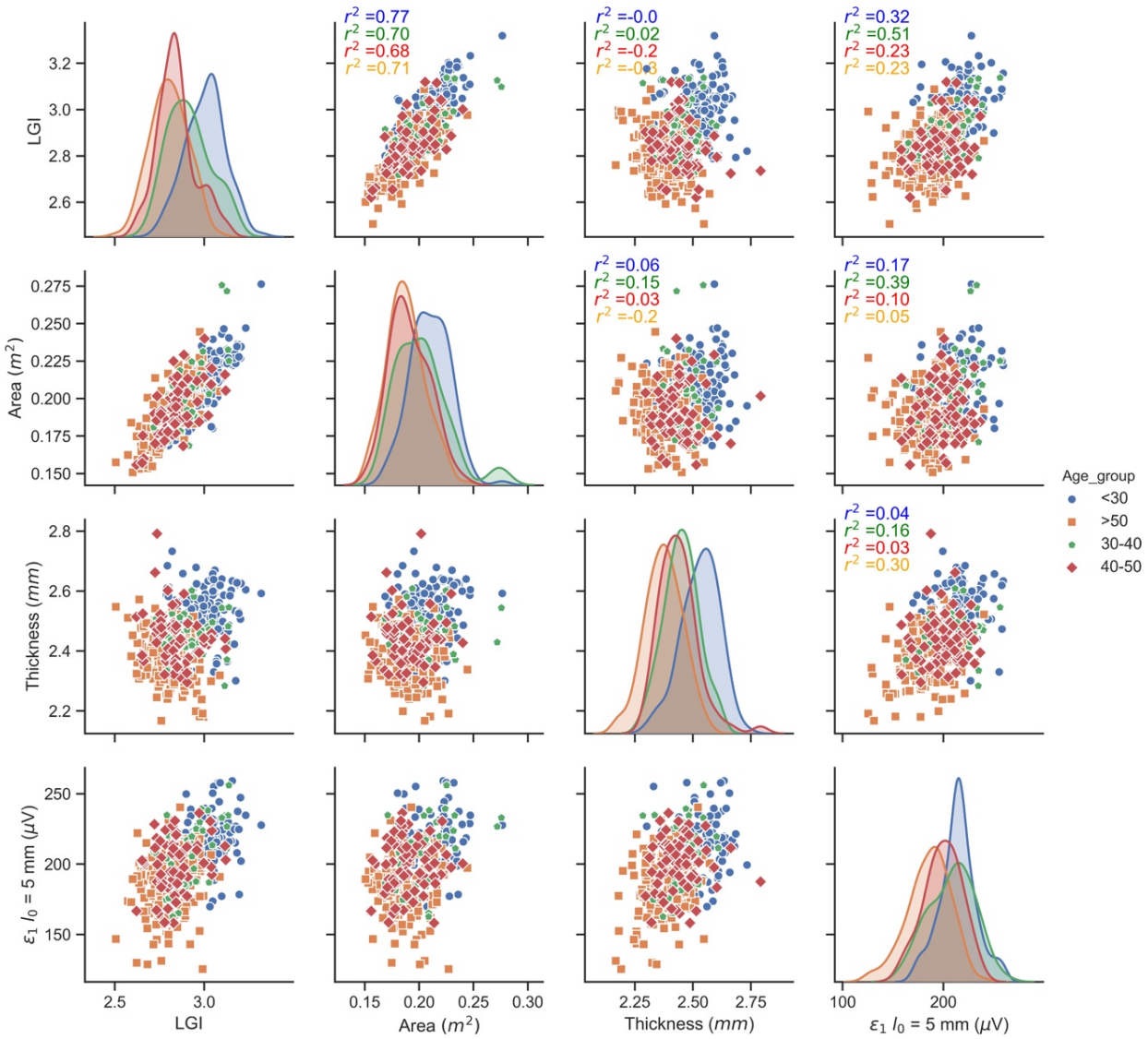

Figure S8: **Correlation between average LGI, EMOD1 (l_0 set to 5 mm), average cortical thickness and total cortical area for different age range groups.** The plots along the main diagonal show histograms of these quantities grouped by age range. The offline range elements show each variable plotted against all others. Pearson correlation coefficients for each pairing, divided by age group, are also presented.

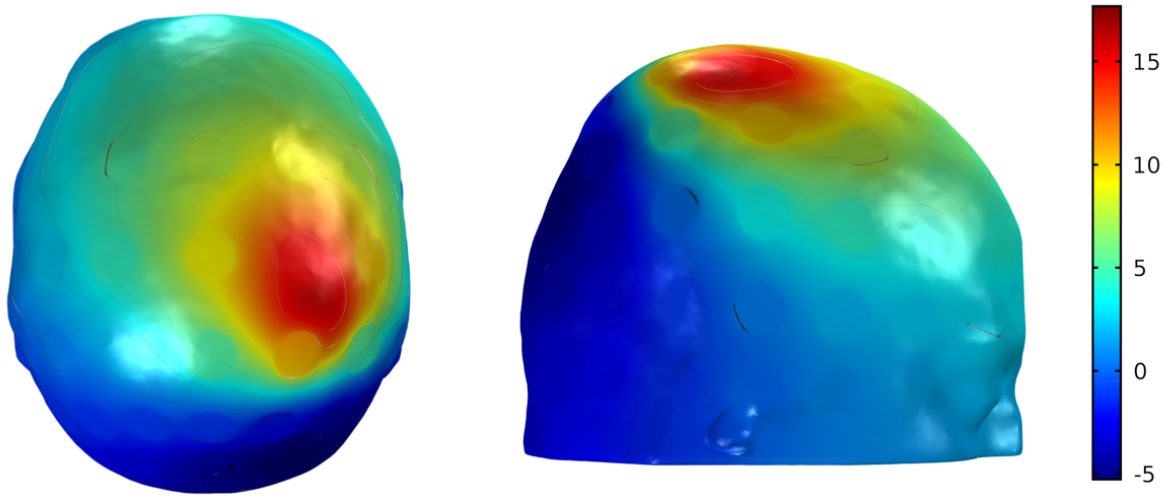

Figure S9: **EEG (referenced to T8, in µV) as generated by cortical patch in Figure 3 (see also Table 1).** The dipole patch consists of 133 dipole sources (patch area of 5.3 cm^2), with a dipole density of 0.5 nAm/mm^2.